

1 **Title:** Top-Down Benchmark of U.S. Methane Inventories Reveals Regional Discrepancies in
2 Activity-Based Estimates

3

4 Authors: John Worden^{1,2,*}, Sudhanshu Pandey^{1,*}, Hannah Nesser¹, Kevin Bowman¹, Colin
5 Harkins^{4,8}, Congmeng Lyu^{4,8}, Joannes D. Maasackers⁵, Deborah Gordon⁶, Daniel Jacob³, Lucas
6 Estrada³, Daniel J. Varon^{9,3}, James D. East³, Lauren Schmeisser⁶, and Zhen Qu⁷

- 7 1. Jet Propulsion Laboratory, California Institute of Technology, Pasadena, California,
8 United States
- 9 2. Joint Institute for Regional Earth System Science and Engineering, University of
10 California, Los Angeles, Los Angeles, California, United States
- 11 3. Harvard University, Cambridge, Massachusetts, United States
- 12 4. NOAA Chemical Sciences Laboratory, Boulder, Colorado, United States
- 13 5. SRON Netherlands Institute for Space Research, Leiden, The Netherlands
- 14 6. Rocky Mountain Institute, Boulder, Colorado, United States
- 15 7. North Carolina State University, Raleigh, North Carolina, United States
- 16 8. Cooperative Institute for Research in Environmental Sciences, University of Colorado
17 Boulder, Boulder, Colorado, United States
- 18 9. Massachusetts Institute of Technology, Cambridge, Massachusetts, United States

19 *These authors contributed equally to the work.

20 * Correspondence to: John Worden jworden@g.ucla.edu

21

22 Abstract: Robust estimates of methane emissions are critical for understanding their impacts on
23 atmospheric warming and air quality, and for assessing methane mitigation strategies. Gridded
24 inventories, such as the U.S. Environmental Protection Agency’s Greenhouse Gas Inventory
25 (EPA GHGI), the Emissions Database for Global Atmospheric Research (EDGAR 2024), and
26 the National Oceanic and Atmospheric Administration’s Fossil Fuel Oil and Gas inventory
27 (NOAA FOG), are constructed to evaluate large-scale emission patterns and support identifying
28 emission mitigation priorities and prioritizing future measurements. However, substantial
29 differences across inventories complicate such assessments. We benchmark EPA GHGI,
30 EDGAR 2024, and NOAA FOG against flux estimates from an atmospheric inversion of
31 Greenhouse Gases Observing Satellite (GOSAT) data from 2012 to 2020 over the Contiguous
32 United States (CONUS). A key technical challenge is the heterogeneous sensitivity of satellite-
33 derived fluxes, which depends on measurement uncertainty, coverage, and inversion model
34 configuration. We account for this heterogeneity by applying an inversion operator to each

35 inventory prior to comparison with the GOSAT-based estimates. The GOSAT estimates are most
36 sensitive to oil&gas and livestock emissions; oil and gas emissions are consistent with NOAA
37 FOG (14.1 Tg CH₄ yr⁻¹ in 2015), but exceed EPA GHGI and EDGAR, particularly across Texas,
38 Oklahoma, and Louisiana. GOSAT-based livestock emissions exceed EPA GHGI and EDGAR
39 by 1–2 Tg CH₄ yr⁻¹, with the largest differences in the Midwest and California. Despite these
40 discrepancies, both activity and satellite based estimates show no observable trends from 2012 to
41 2020 in fossil and livestock emissions.

42
43

44 1. Introduction

45

46 All GOSAT-derived emissions and corresponding inputs/algorithms are available at
47 [<https://doi.org/10.5281/zenodo.15786798>].
48 Jupyter / python code at [<https://zenodo.org/records/16921536>] shows how to compare these
49 GOSAT derived emissions to inventories.

50

51 Methane is a potent greenhouse gas that plays a significant role in atmospheric warming
52 (Saunio et al., 2020). Methane is emitted from multiple anthropogenic sources including
53 livestock, oil and gas exploitation, manure, rice cultivation, wastewater, solid waste, and coal
54 mining, and from natural sources, particularly wetlands. Methane is also the main component of
55 natural gas, a valuable global commodity that can pose safety risks when it leaks. Accurate and
56 verifiable estimates of its emissions are essential for tracking progress and guiding effective
57 mitigation strategies, and for accounting for the economic value of energy waste (IEA, 2025;
58 World Bank, 2025). Gridded methane emission inventories, such as the gridded United States
59 Environmental Protection Agency’s Greenhouse Gas Inventory (EPA GHGI), the Emissions
60 Database for Global Atmospheric Research 2024 release (EDGAR 2024), and the National
61 Oceanic and Atmospheric Administration’s Fuel-based Oil and Gas inventory (NOAA FOG), are
62 widely used for comparing sectoral emissions, primarily at the regional scale, to atmospheric
63 data (EPA, 2021; Maasackers et al., 2023; Crippa et al., 2020, 2024; Francoeur et al., 2021,
64 Kruskamp *et al.* 2025 <https://zenodo.org/records/16782735>). However, discrepancies in

Deleted: economic

66 how the inventories are generated, e.g. from emission factor assumptions, activity data, and/or
67 spatial proxies and resolution can result in substantial variation in both the magnitude and
68 sectoral attribution of emissions (Hristov et al. 2017; Alvarez et al., 2018; Maasakkers et al.,
69 2021; Petrescu et al. 2024; Gordon 2025). In some cases, differences between inventories can be
70 as large as the emissions themselves (Figure 1), complicating the evaluation of national and
71 regional emission trends. Verification of their underlying parameterizations is often limited by
72 spatiotemporal mismatches between empirical measurements and inventory assumptions.
73 Moreover, differences between activity-based emissions and flux estimates based on
74 observations combined with atmospheric modeling (e.g., top-down atmospheric inversions) can
75 far exceed the changes inferred from the observed growth in atmospheric methane concentrations
76 (Nisbet et al., 2019; Worden et al., 2022). As a result, tracking mitigation progress using bottom-
77 up inventories alone could be unreliable without independent observational constraints. In
78 addition to these uncertainties, emissions missing in the inventories pose another significant
79 challenge. For instance, sporadic high emitters in both fossil fuel production and waste
80 management, often caused by mechanical failures, may not be captured in traditional inventories
81 (Cusworth et al., 2020, 2024; Sherwin et al., 2024); consequently, the magnitude of these
82 emissions remains poorly understood.

83 To evaluate potential uncertainties in bottom-up inventories, top-down emissions
84 estimates derived from satellite observations, such as those from the Greenhouse Gases
85 Observing Satellite (GOSAT), provide a valuable, independent constraint. These atmospheric
86 measurements inherently capture all emissions influencing methane concentrations, including
87 unreported or underestimated sources, and therefore offer a more comprehensive view of total
88 methane emissions. However, the resulting estimates and their information content (spatial
89 resolution + uncertainties) depend strongly on the observational sampling, sensitivity of the
90 observation to the emissions, choice of a priori fluxes, and the inversion regularization.
91 Consequently, over regions with limited sampling, e.g., due to clouds or low sunlight, top-down
92 analyses have greatly reduced sensitivity to nearby emissions, so the estimates there simply
93 reflect the *a priori*. In contrast, emissions inferred for regions with ample sampling are more
94 likely to accurately represent local sources. The focus of this paper is to demonstrate how this
95 GOSAT-based benchmark can be used to evaluate alternative gridded inventories while
96 accounting for its variable information content as discussed next.

98 Method and Data

99 **Accounting for choice of *a priori* and inversion regularization:** Comparisons between
 100 satellite-based top-down fluxes and activity-based inventories must account for the variation in
 101 sensitivity of the data to emissions and choice of *a priori*, otherwise substantial uncertainty (also
 102 known as *smoothing error*) is introduced into the comparison (Rodgers, 2000; Worden et al.,
 103 2022, 2023). Smoothing error in this context can be mitigated for these comparisons by at least
 104 three ways: 1) by using the inventory as the *a priori* in the inversion or 2) by applying an
 105 inversion operator to the inventory being compared (the inversion operator depends on the
 106 inversion *a priori* and what is called the averaging kernel matrix, Appendix B) or 3) by adjusting
 107 the GOSAT based estimate using the gridded inventory and the averaging kernel matrix to
 108 replace the effect of the original prior (also known as prior swapping).

109 In the first scenario, recalculating the inversion and subsequently comparing to the *a*
 110 *priori* is computationally expensive (e.g., Nesser et al., 2024 and references therein) as it
 111 involves minimizing a cost function of gridded emissions vector (e.g. \mathbf{z}) that typically has the
 112 following form:

$$113 \quad \mathbf{C} = \|\mathbf{y} - \mathbf{F}(\mathbf{z}_A)\|_{\mathbf{S}_n}^2 + \|\mathbf{z} - \mathbf{z}_A\|_{\mathbf{S}_A}^2 \quad (1)$$

114 Where \mathbf{y} is a state vector representing concentrations (e.g. total column methane or $X\text{CH}_4$), the
 115 forward model $\mathbf{F}(\mathbf{z}_A)$ in this case is the Goddard Earth Observing System – Chemistry model
 116 (GEOS-Chem) driven by a distribution of *a priori* emissions (\mathbf{z}_A). The matrix \mathbf{S}_n represents the
 117 measurement error covariance for the total column data and the matrix \mathbf{S}_A represents the
 118 uncertainty (or covariance) in our *a priori* emissions. For the benchmark described in this paper,
 119 the vector \mathbf{z} represents the spatial distribution of anthropogenic emissions by sector, in this case
 120 livestock, waste, coal, rice, oil&gas. Wetlands and fire emissions are also estimated with the
 121 GOSAT data and the effect of jointly estimating these emissions are included in the posterior
 122 covariance and uncertainties of the anthropogenic emissions estimate (Worden *et al.* 2022;
 123 2023).

124 The estimate for the converged solution, \mathbf{z} , can be related to the “true distribution” of the
125 emissions (\mathbf{z}) with the following (e.g. Rodgers 2000).

$$126 \quad \mathbf{z} = \mathbf{z}_A + \mathbf{A}(\mathbf{z} - \mathbf{z}_A) \quad (2)$$

127

128 where for clarity we have not included the uncertainty terms (see Appendix B). The averaging
129 kernel matrix \mathbf{A} is a function of the *a priori* and posterior covariance, \mathbf{Z} and \mathbf{Z}_A (see Appendix B
130 for a description of uncertainties and prior covariances) and describes the sensitivity of the
131 distribution of estimated emissions to the true state ($\mathbf{A} = \frac{\partial \mathbf{z}}{\partial \mathbf{z}}$). Approach #2, which is to apply an
132 inversion operator to the inventory, is equivalent to replacing \mathbf{z} , or the “true distribution” of
133 emissions, with the alternative inventory, \mathbf{z}_I in Equation 1; this approach is commonly used for
134 data assimilation or for comparing atmospheric trace gas profiles from models or in situ
135 measurements to remotely sensed measurements (e.g. Wecht *et al.* 2014, Herman *et al.* 2014).
136 This revised estimate can be compared to \mathbf{z} while accounting for the *a priori* and regularization
137 choices made in the inversion described by Equation 1. Approach #3 (or prior swapping) instead
138 involves replacing \mathbf{z}_A with the alternative inventory (e.g. Rodgers and Connor 2003)

139

$$140 \quad \mathbf{z}_{new} = \mathbf{z} - (\mathbf{I} - \mathbf{A})\mathbf{z}_A + (\mathbf{I} - \mathbf{A})\mathbf{z}_I \quad (3)$$

141 And is equivalent to re-running the inversion described by Equation (1) with this alternative *a*
142 *priori*.

143 As approaches 2 and 3 are linear operations, they result in equivalent comparative differences as
144 shown in Appendix B. In this manuscript we use the inversion operator approach (Equation 2)
145 for consistency with previous publications (e.g. Worden *et al.* 2022; 2023).

146 **Sector Based Attribution:** We use estimates of gridded integrated fluxes from a GEOS-Chem
147 based inversion using GOSAT XCH₄ data as described in Qu *et al.* (2022,2024). We use a
148 Bayesian-based sectoral partitioning approach (Appendix A, Worden *et al.*, 2022, 2023) to
149 project these top-down integrated fluxes to emissions by sector at a 1° × 1° resolution. This
150 approach characterizes the inversion solution by providing a posterior covariance for the solution
151 and provides the “inversion operator” (Equation 2) that, when applied to a gridded inventory,

152 enables the comparison to inversion results by capturing the influence of the inversion’s prior
153 emissions and the sensitivity of the satellite observations to those emissions (Rodgers, 2000).

154

155 **Inventories:** (See Appendix C for more detail) The inventories we compare include EDGAR
156 2024 (Crippa et al. 2024), the [gridded U.S. EPA GHG inventory](#) (GHGI) (Maasackers et al.
157 2023), and NOAA FOG (Francoeur et al. 2021). The EDGAR and GHGI inventories provide
158 information about methane emissions across multiple sectors (e.g., livestock, waste, oil and gas,
159 coal, rice). The approaches estimating these emissions vary, with EDGAR down-scaling national
160 totals to finer scales using spatial information about the sources using global datasets while the
161 GHGI gridded inventory reflects emission factors and activity data used in the EPA U.S.
162 Greenhouse Gas Inventory. In contrast, NOAA FOG focuses specifically on fossil methane
163 emissions and is a hybrid inventory that integrates atmospheric CH₄ and NO₂ observations with
164 activity-based NO₂ metrics (Francoeur et al. 2021). While these inventories show considerable
165 overlap in the location of emissions, differences can be large, even when aggregating from the
166 original 0.1 degree grid of the inventories to the 1 degree grid shown for Figure 1.

167

168 As stated previously, our goal for this study is to demonstrate a benchmark for U.S.
169 methane emission gridded inventories and their changes from 2012 to 2020. These comparisons
170 are documented [and publicly accessible at Zenodo \(see data availability\)](#); Jupyter notebooks are
171 provided [here](#) that demonstrate how to compare gridded inventories to GOSAT-based emissions.
172 These benchmarks will be updated as newer datasets, such as inverse analyses using Sentinel-5P
173 TROPOMI (Tropospheric Ozone Monitoring Instrument) observations, become available (e.g.,
174 Nesser et al. 2024; Hancock et al. 2025). Readers unfamiliar with the Bayesian attribution
175 framework, the GOSAT inversion, or the specific inventories compared are encouraged to
176 consult the appendices, where these methods are summarized, or our previously published work
177 on the subject (Cusworth et al. 2021; Worden et al. 2022,2023).

178

179 2. Integrated total and sectoral USA emissions for 2015

180

Deleted: EPA based Greenhouse Gas Inventory

Deleted: through

Deleted: Worden and Pandey 2025; Pandey and Worden
2025) (<https://doi.org/10.5281/zenodo.15786797>,
<https://doi.org/10.5281/zenodo.16921536>);

Deleted: in the Pandey and Worden link

187 Table 1 summarizes U.S. methane emissions by sector for 2015, based on the GOSAT
 188 data and the sectoral attribution approach described in this study (Appendix A). The error
 189 characterization (Appendix B) includes uncertainties from the *a priori* as well as measurement
 190 and model systematic error. The prior emissions are taken from Worden *et al.* (2023). Table 1
 191 also shows a quantity called the Degrees of Freedom for Signal (DOFS), which is given by the
 192 trace of the averaging-kernel matrix for the corresponding state-vector elements in \mathbf{z} . The DOFS
 193 describe the extent to which the estimate is informed by observations rather than prior
 194 assumptions (Appendix B), as well as the spatial information content. For example, from
 195 Equation 2, if $\mathbf{A} \approx \mathbf{0}$ (equivalent to DOFS = 0), observations say essentially nothing about the
 196 emissions and the estimate reduces to the prior. If \mathbf{A} is the identity matrix, then the DOFS equals
 197 the number of state-vector elements and the estimate exactly reflects the true distribution,
 198 modified by the expected uncertainties (Appendix B). The DOFS reported in Table 1 refer to the
 199 spatially distributed estimate, not for the total emissions value. Hence, DOFS > 1 means there is
 200 at least some spatial information for that sector’s estimate.

201 For this GOSAT-based benchmark, the highest information content is available for total,
 202 livestock, and oil and gas (O&G) emissions, while waste emissions estimates are only
 203 moderately constrained by the data, and rice and coal emissions have limited observational
 204 information. This variability in information content underscores the need for careful
 205 interpretation of top-down estimates, particularly when examining spatial and sectoral patterns or
 206 trends.

207

208 Table 1: GOSAT-Based CONUS Anthropogenic Emissions and Information Content by
 209 Sector (2015)

Sector	Emissions (Tg CH₄/yr)	<i>A priori</i> (Tg CH₄/yr)	DOFS*
Total	29.4 ± 1.5	28.2±2.0	3.4
Livestock	10.3 ± 1.2	9.2 ± 1.4	1.8
Rice	0.4 ± 0.1	0.4±0.1	0.0
Waste	4.5 ± 0.6	5.6±0.8	0.6
Oil & Gas	11.1 ± 0.9	9.9±1.2	1.0

Coal 3.1 ± 0.3 3.1±0.3 0.1

210

211 Table 2 compares our emissions to previous inversions using atmospheric data and to the
 212 inventories discussed in this paper (Appendix C). As can be seen in Table 2, our atmospheric-
 213 based emissions are generally consistent with other studies, typically within 1–2 standard
 214 deviations of the reported uncertainties, even though each study uses different priors, has
 215 different systematic errors, and has different sensitivity to the underlying emissions. These
 216 comparisons also show that total emissions from atmospheric-based inversions are typically
 217 larger than activity-based estimates, with the livestock and oil and gas sectors responsible for
 218 most of the discrepancy.

Formatted: Font: Times New Roman, 12 pt
 Formatted: Indent: First line: 0.5"

219
220

221 Table 2: Comparison of Methane Emissions by Study. All totals are CONUS

222 anthropogenic; years as listed;

223 (All values in Tg CH₄/yr)

Deleted: Table 2 compares these emissions to previous inversions using atmospheric data and with the inventories (Appendix C) discussed in this paper. As can be seen in Table 2, our atmospheric based emissions are generally consistent (within 1-2 sigma of the calculated uncertainty) with other studies, even considering that each study has different priors, systematic errors, and sensitivity of the data to the underlying emissions. These comparisons reveal that the total emissions from the atmospheric-based inversions are typically larger than the activity-based estimates with the livestock and oil&gas sectors responsible for most of the discrepancy.

Study	Total	Livestock	Rice	Waste	Oil & Gas	Coal
(Atmospheric Inversions)						
GOSAT (2015 This Work)	29.4 ± 1.5	10.4 ± 1.2	0.4 ± 0.1	4.6 ± 0.6	11.1 ± 0.9	3.1 ± 0.3
GOSAT (2019) ¹	27.3 ± 3	9.9 ± 0.9	0.3 ± 0.1	4.0 ± 0.7	10.3 ± 1.0	2.8 ± 0.4
TROPOMI (2019) ²	30.9 ± 0.9	10.4 ± 0.3	N/A	6.9 ± 0.6	10.4 ± 0.3	1.5 ± 0.4
GOSAT + Surface (2009–2020) ³	29.1 ± 0.5	8.8 ± 0.3	N/A	4.2 ± 0.1	14.1 ± 0.2	2 ± 0.4
GOSAT (2010–2015) ⁴	31 ± 1.0	9.4 ± 0.4	0.4 ± 0.2	6.2 ± 0.2	11.1 ± 0.6	3.2 ± 0.1
In Situ (2007-2008) ⁵	33.4 ± 2	N/A	N/A	N/A	N/A	N/A
In Situ (2003) ⁶	32.4 ± 5	N/A	N/A	N/A	N/A	N/A
(Activity Models and Year)						
GHGI (2015) ⁷	23.7 ± 2.1	8.9 ± 1.4	0.6 ± 0.3	4.8 ± 1.4	6.9 ± 1	2.5 ± 0.4
EDGAR (2015) ⁸	25.7 ± 2.1	8.6 ± 1.4	0.3 ± 0.1	4.3 ± 1.3	10.1 ± 1	2.4 ± 0.4

NOAA FOG (2015)⁹

14.1 ± 2

Table 2: Comparison of Methane Emissions by Study. All totals are CONUS anthropogenic emissions for the years listed. Values are reported in Tg CH₄ yr⁻¹. Atmospheric inversions exclude natural sources and fire emissions where sectoral separation is available. Activity-based estimates include the gridded EPA GHGI, EDGAR 2024, and NOAA FOG inventories evaluated in this study. References: (1) Worden et al. (2022), (2) Nesser et al. (2024), (3) Janardanan et al. (2024), (4) Maasakkers et al. (2019), (5) Miller et al. (2013), (6) Kort et al. (2008), (7) Maasakkers et al. (2016, 2023), (8) Crippa et al. (2024), and (9) Francoeur et al. (2021).

Formatted: Font: Times New Roman, 12 pt

Deleted: Table 2 lists emissions from several atmospheric-based inversions, excluding natural sources and fire emissions, as well as from the gridded EPA GHGI, EDGAR 2024, and FOG inventories. References: (1) Worden et al. 2022, (2) Nesser et al. 2024, (3) Janardanan et al. (2024), (4) Maasakkers et al. (2019), (5) Miller et al. (2013), (6) Kort et al. (2008), (7) Maasakkers et al. (2016, 2023), (8) Crippa et al. (2024), (9) Francoeur et al. (2021).

2.1 Oil and Gas Emissions (GOSAT, FOG, EPA, and EDGAR)

We next compare the GOSAT-based emissions for O&G to those from NOAA FOG, GHGI, and EDGAR inventories. In particular, we demonstrate how applying the inversion operator to these inventories modifies our interpretation of the comparison.

Spatial Distribution for 2015: Figures 2 through 4 compare the spatial distribution of U.S. oil and gas (O&G) methane emissions in 2015 from the GOSAT inversion with those from the FOG, GHGI, and EDGAR (2024 release, Crippa et al., 2024) inventories respectively. These comparisons demonstrate the importance of accounting for the varying information content of the GOSAT inversion, which is influenced by both the prior emissions used in the inversion and the sensitivity of the aggregated satellite observations to underlying emission patterns (Worden et al., 2023 and references therein). In Figure 2, the upper left panel (a) shows the GOSAT based estimate. The upper right panel (b) shows the original FOG emissions. The middle left panel (c) shows the difference between the top two. The middle right panel shows the difference between FOG emissions and GOSAT based emissions after applying the inversion operator (denoted AK). All figures use 1x1 degree gridding. The bottom right panel (E) shows the diagonal of the averaging kernel (or DOFS) corresponding to that location for oil and gas emissions. As seen in the left panel of Figure 2, significant regional discrepancies between the GOSAT and FOG inventories exist, with similar magnitude differences as shown in Figure 1. However, after

274 applying the inversion operator (Equation 2) to the FOG inventory (labeled FOG AK), many of
275 these differences are greatly reduced (middle right panel)

276 Small differences between GOSAT and the inventory, after applying the inversion operator, can
277 also occur because of limited sensitivity, as indicated by the DOFS, for example over the Bakken
278 region of North Dakota. As discussed previously and shown in Equation 2 and Appendix B, in
279 such cases the difference between the GOSAT estimate and the inventory adjusted by the
280 inversion operator should be close to zero, because both terms reduce to $\sim z_A$. In contrast, the
281 GOSAT estimate shows increased sensitivity to emissions in Oklahoma, Texas, and Louisiana.
282 Based on this comparison, and on the integrated total emissions in the next section, we conclude
283 that the GOSAT estimate does not falsify the spatial distribution of methane emissions posited
284 by the FOG oil and gas inventory.

285

286 **Interpreting Comparisons between GOSAT, EDGAR, and GHGI emissions:**

287

288 Comparisons between GOSAT and EDGAR (Figure 3) and between GOSAT and EPA GHGI
289 (Figure 4) show larger discrepancies, even after applying the inversion operator, particularly in
290 northwest Colorado, Texas, Oklahoma, and Louisiana. These patterns indicate substantial
291 inventory uncertainties in well-observed regions with intensive oil and gas activity. Some
292 regions are sparsely observed by GOSAT, so their contributions may be important but their
293 uncertainties cannot be reliably assessed with this benchmark. When measurement cost is a
294 constraint, the discrepancy hotspots identified here are high-value targets for additional
295 observations, with expanded coverage of under-sampled regions as resources allow.

296

297 Previous studies (e.g., Alvarez et al. 2018; Cusworth et al. 2022; Sherwin et al., 2024)
298 have shown that a small number of high emitters (e.g., <2%; Sherwin et al., 2024), likely due to
299 unplanned mechanical failures, contribute disproportionately to the fossil methane budget. These
300 sources are likely underrepresented or missing from activity-based inventories. The agreement
301 between FOG and GOSAT supports this conclusion, as the FOG inventory integrates
302 atmospheric CH₄ with NO_x observations and activity metrics; these regional CH₄ observations
303 capture emissions under-represented in purely bottom-up approaches. If such super-emitters are

304 entirely responsible for the discrepancies between GOSAT and the EPA GHGI and EDGAR
305 inventories, then comparisons between the GOSAT, EPA, EDGAR, and FOG O&G emissions in
306 Table 2 suggest these sources are undercounted by ~ 7 Tg CH₄/yr of reported natural gas
307 emissions, far exceeding previous estimates, as previously documented in other studies (e.g.,
308 Alvarez et al. 2018; Cusworth et al. 2022; Sherwin et al., 2024; Zavala-Araiza et al. 2015).

309
310

311 **Integrated totals for 2015:** Figure 5 compares integrated total oil and gas (O&G) emissions
312 derived from GOSAT with those from the FOG, GHGI, and EDGAR inventories.

313 Before applying the inversion operator, total FOG emissions are estimated at 14.1 ± 2 Tg CH₄
314 yr⁻¹. We assumed the same prior covariance structure (\mathbf{Z}_A , Appendix B; Worden et al., 2022,
315 2023) for FOG as for the GOSAT *a priori*. This yields a smaller total uncertainty (2 Tg CH₄ yr⁻¹)
316 than the ~ 2.8 Tg CH₄ yr⁻¹ uncertainty for total FOG O&G emissions inferred from a Monte Carlo
317 analysis of NO_x activity data (Francoeur *et al.*, 2021). Using a different covariance structure that
318 is consistent with the stated uncertainty in total emissions could therefore change conclusions
319 about whether the GOSAT estimate falsifies the FOG inventory, and the inversion-operator
320 methodology in Equation 2 would allow this. However, a full covariance is required, with
321 explicitly computed off-diagonal terms such that, when projected to a single number, it
322 reproduces the expected uncertainty reported in, for example, Francoeur et al. (2022).

323 After applying the inversion operator, the FOG total is reduced to 11.4 Tg CH₄ yr⁻¹. The
324 uncertainty shown for the modified FOG estimate (denoted FOG-AK) reflects the uncertainty in
325 the difference between the GOSAT-based estimate and the FOG-AK estimate (Appendix B
326 Equation 15), not the uncertainty of the FOG-AK estimate itself. Because the FOG-AK estimate
327 is consistent with the GOSAT-based inversion within the reported uncertainty, this comparison
328 suggests that the GOSAT estimate does not falsify the original, higher FOG total of 14.1 Tg CH₄
329 yr⁻¹.

330 Figure 5 also shows comparisons to GHGI and EDGAR. For these inventories, uncertainties
331 prior to applying the inversion operator are derived using the same prior covariance structure as
332 for the GOSAT a priori, because published full covariances are not readily available.

333 In contrast to the FOG comparison, both the EPA and EDGAR estimates, with or without
334 application of the inversion operator, are inconsistent with the GOSAT-based inversion. Their
335 differences lie well outside the post-operator uncertainty shown for each inventory. As shown in
336 Figures 3 and 4 these differences are spatially located primarily in the Texas, Oklahoma, and
337 Louisiana regions. As noted previously, additional measurements here are therefore likely to
338 reduce uncertainties in the USA O&G methane budget.

339
340 **Integrated Totals: 2012–2020:** Figure 6 shows annual methane emissions from 2012 to 2020.
341 Despite substantial increases in oil and gas production over this period, all gridded inventories
342 and the GOSAT top-down estimates show no significant change in total U.S. methane emissions,
343 although the FOG inventory may have a slight increase. This apparent disconnect between rising
344 production and stable emissions has been noted in several studies and is commonly attributed to
345 improvements in production efficiency, leak detection, and emissions control technologies (e.g.,
346 Lu et al., 2023). EPA GHGI supports this conclusion, showing relatively flat changes in fossil
347 fuel methane emissions over the same period. This stability in the activity estimate is explained
348 by offsetting trends, including a decline in exploration emissions due to fewer well completions,
349 the adoption of lower-emitting equipment, and stable or slightly declining well counts
350 (Maasakkers et al. 2023). For instance, while natural gas production increased by 26% and crude
351 oil production by 67%, the number of active gas and oil wells remained roughly constant,
352 declining slightly over the period. Emissions from gas systems were flat overall, with increases
353 in gathering and boosting offset by decreases in production and processing. Similarly, petroleum
354 system emissions rose by just 11% due to a significant drop in exploration-related emissions
355 (Maasakkers et al. 2023).

356

357 *2.2 Livestock Emissions (GHGI and EDGAR)*

358

359 **Spatial Distribution for 2015:** Similar to Figures 2-4, Figures 7 and 8 show the spatial
360 distribution of livestock methane emissions from GOSAT, EDGAR, and GHGI data. The FOG
361 inventory is limited to oil and gas emissions and is therefore excluded from this and subsequent
362 comparisons. Methane emissions from livestock generally scale with herd size, particularly dairy
363 and beef cattle. Dairy cows typically emit more than twice as much methane as beef cows, due to
364 higher enteric fermentation (Wolf et al., 2017; Hristov et al., 2017). Emissions vary
365 geographically with management and environmental conditions (for example grazing
366 practices, feed quality, and temperature, Wolf et al., 2017). Inventories account for this
367 using region-specific emission factors, but if the factors used are not representative of
368 actual local conditions, the resulting difference between the atmospheric based and activity
369 based emissions should be spatially structured rather than random. Consistent with this,
370 we observe systematic regional biases relative to the GOSAT-based estimates: inventories
371 in California and the northern states are higher than GOSAT, whereas inventories in
372 northern Texas are lower.

373
374 **Integrated Total for 2015:** Figure 9 compares integrated livestock methane emissions from
375 GOSAT with GHGI and EDGAR inventories, each shown with and without the inversion
376 operator applied. The GHGI and EDGAR totals differ modestly. The EPA total lies slightly
377 outside the GOSAT uncertainty range, while the EDGAR total falls within it. However,
378 agreement in totals does not imply agreement in spatial patterns. For EDGAR in particular,
379 closer total agreement with GOSAT coincides with offsetting regional deviations, with positive
380 differences in parts of the Midwest and negative differences in California. These cancellations
381 reduce the apparent mismatch in the national total, which underscores the importance of
382 evaluating spatial variability alongside integrated totals. Overall, comparisons of integrated
383 totals and spatial patterns indicate substantial remaining uncertainty in livestock emissions.
384 Additional measurements over California and the Midwest, especially in the Texas and
385 Oklahoma region, would likely reduce this uncertainty.

386
387 **Integrated Totals for 2012-2020:** Figure 10 (and Table 2) shows comparisons between the
388 integrated total livestock emissions from the GOSAT based inversion and the GHGI and
389 EDGAR inventories. The GOSAT-based estimate as well as those from the GHGI and EDGAR

390 inventories do not observably change within the calculated uncertainties, except possibly for the
391 year 2019. We therefore conclude that GOSAT based livestock emissions cannot falsify the
392 posited (flat) trends from activity data (Maasakkers et al. 2021).

393

394 2.3 Waste (GHGI and EDGAR)

395 Figures 11 and 12 show the spatial distribution of methane emissions from the waste
396 sector based on GOSAT, GHGI, and EDGAR estimates and Figure 13 shows the integrated total
397 for 2015. The largest differences are for California for the EDGAR / GOSAT comparison. The
398 integrated waste sector methane emissions from GOSAT are estimated at 4.5 ± 0.6 Tg CH₄/yr,
399 while both GHGI and EDGAR report lower values of 4.2 ± 0.3 Tg CH₄/yr. These differences are
400 not statistically significant, as the GOSAT estimate lies within the uncertainty range of both
401 inventories (after applying the inversion operator). However, there is very limited spatial
402 information content in the GOSAT waste estimate (~0.6 DOFS total). Consequently, the spatial
403 differences shown in the right-bottom panel don't show meaningful differences between the
404 inventories and the GOSAT waste estimate for most of the country. Because of this limited
405 sensitivity we do not compare temporal changes in the waste emissions.

406

407 3. Summary and Future Directions

408

409 Top-down methane emissions estimates vary in their information content depending on
410 the emission sector and observing system. For these GOSAT based emissions estimates,
411 information content is greatest for oil and gas and livestock, so these sectors are best suited for
412 inventory evaluation using the results shown here. Waste, coal, and rice exhibit lower
413 information content in this analysis because GOSAT does not adequately sample methane
414 variability attributable to those sources. Even so, our information-content-based comparison
415 identifies where additional measurements would yield the largest uncertainty reductions in
416 gridded inventories.

417 In particular, our results highlight the need for targeted measurement campaigns,
418 especially in the Texas, Oklahoma, and Louisiana drilling basins, where additional data can most
419 effectively reduce inventory uncertainties. For the livestock sector, California and Northern

420 Texas stands out as key regions where improved activity based and atmospheric methane
421 observation can have the highest impact. These findings underscore the importance of
422 prioritizing high-emitting or uncertain regions to refine national methane budgets.
423 Beyond regional targeting, improving inversion resolution is also key. Higher-resolution flux
424 estimates, whether through satellites like TROPOMI or plume-resolving instruments (e.g., Jacob
425 et al. 2022; Pandey et al. 2025 and refs therein), are particularly needed for sectors such as waste,
426 coal, and oil and gas, where coarse-resolution inversions struggle to isolate source signals. In
427 particular, integrating plume-resolving and area-flux estimates enhances the sectoral attribution
428 of emissions and improves the information content for inventory evaluation (Pandey *et al.* 2025).

429
430 **(Trends)** Inversions conducted using GOSAT data and GEOS-Chem (see references in
431 Table 2), show no discernible trend over the analysis period, which is consistent with all three
432 gridded inventories discussed in this manuscript. However, the fact that other inversions show
433 different trends highlights the importance of benchmarking approaches (Janardanan et al. 2024),
434 not only for validating inventories but also for identifying uncertainties in inversion outputs
435 themselves. These differences matter for informing effective remediation strategies and setting
436 realistic expectations for emission reductions.

437 As satellite constellations improve in spatial resolution, sampling, and accuracy, top-
438 down flux estimates become more accurate at higher spatial resolution (e.g., Jacob et al., 2022).
439 Using TROPOMI, Nesser et al. (2024) produced a 2019 North American emissions map with a
440 degree of freedom for signal (DOFS) of ~772, more than two orders of magnitude higher than in
441 our GOSAT record, driven by a similar increase in observations. This resolution enables explicit
442 estimation of many large sources, including landfills. East et al. (2025) extended this approach to
443 global coverage at similar ~25 km gridding. Building a benchmark from the combined record
444 will help evaluate how countries have managed emissions before and after the Global Methane
445 Pledge, which targets a 30 percent reduction from 2020 to 2030. Our approach shows how
446 inventories can be benchmarked against these improved flux estimates to reduce uncertainty,
447 especially smoothing error, without re-running inversions with inventory priors. Combining
448 high-resolution, independent datasets will support more accurate methane inventories, clarify
449 source trends, and inform effective mitigation strategies.

450 **Appendices**

451 **Appendix A: GOSAT Methane Fluxes and Projection to USA Emissions by Sector**

452 **(Overview)** Yearly sectoral emissions by region based on the satellite data are generated in a two
453 step process. The first step is to quantify global integrated fluxes using total atmospheric column
454 methane data from the Japanese GOSAT (Greenhouse gases Observing SATellite) instrument
455 (Parker *et al.* 2011) and the GEOS-Chem model (Zhang *et al.*, 2021). The approach used to
456 generate fluxes has been extensively documented in past literature (e.g. Zhang *et al.*, 2021, Qu *et al.*,
457 2024), and we refer the reader to these articles. The state vector for this inversion include 1)
458 yearly anthropogenic methane emissions between 2010 and 2022 at a gridding of 5x4 degrees
459 (longitude/latitude) and we use the estimates between 2012 and 2020 for this study, 2) wetland
460 methane emissions for specified regions for each month between 2010 to 2022), and 3) the
461 yearly hemispheric methane sink. The second step (next section) is a linear estimate based on an
462 optimal estimation sectoral emissions attribution approach (Cusworth *et al.* 2021; Worden *et al.*
463 2022) that projects the integrated anthropogenic fluxes to emissions by sector and trends at the
464 same 5x4 degree gridding and then again at 1x1 degree (lon/lat) gridding over the USA. This
465 projection accounts for the prior distribution and uncertainties in the emissions (e.g. Worden *et al.*
466 2022). We next provide more detail on projection/attribution methodology as it is relevant to
467 the benchmarking methodology that is the focus of this paper.

468 **(Sectoral attribution of fluxes to emissions)** We use a Bayesian based approach to project the
469 fluxes described in the previous section (at 5x4 degrees lon/lat) to emissions by sector at 1x1
470 degree. The full methodology is described in Cusworth *et al.* (2021) and first applied to methane
471 fluxes in Worden *et al.* (2022) and again in Worden *et al.* (2023). This approach is equivalent to
472 swapping the *a priori* assumptions, given by \mathbf{x}_A and \mathbf{S}_A , to a different state vector \mathbf{z}_A (and *a priori*
473 covariance \mathbf{Z}_A) when a linear relationship between the different state vectors \mathbf{x} and \mathbf{z} exist. The
474 approach provides the full posterior and prior covariances and priors needed to account for the
475 varying information content of satellite based emissions estimates when comparing these
476 emissions to either each other (e.g. between years) or to inventories (Worden *et al.* 2023) or to
477 other estimates. We refer the reader to these papers, starting with Cusworth *et al.* (2021) for the
478 primary derivation, and summarize here.

479

480 Given a linear mapping between one state vector and another (e.g. between fluxes \mathbf{x} at 5x4
481 degrees versus emissions \mathbf{z} at 5x4 degrees or alternatively emissions at 1x1 degree):

482

$$483 \mathbf{x} = \mathbf{Mz}, \quad (4)$$

484

485 As discussed in Worden et al. (2023), the solution for projecting fluxes back to emissions takes
486 the form:

487

$$488 \mathbf{z} = \mathbf{z}_A + \mathbf{ZM}^T \mathbf{S}^{-1} [(\mathbf{I} - \mathbf{S}\mathbf{S}_A^{-1})(\mathbf{x}_A - \mathbf{Mz}_A) + (\mathbf{x} - \mathbf{x}_A)] \quad (5)$$

489

490 where the \mathbf{z} and \mathbf{z}_A is the posterior and prior emissions state vector respectively with posterior
491 and prior error covariance \mathbf{Z} , \mathbf{Z}_A respectively.

492

493 The posterior emission error covariance matrix \mathbf{Z} is calculated explicitly given \mathbf{M} , \mathbf{S}_A , \mathbf{S} , and
494 prior emissions error covariance matrix \mathbf{Z}_A :

495

$$496 \mathbf{Z} = (\mathbf{M}^T (\mathbf{S}^{-1} - \mathbf{S}_A^{-1}) \mathbf{M} + \mathbf{Z}_A^{-1})^{-1} \quad (6)$$

497

498

499 Here, the \mathbf{S} is the posterior covariance for the fluxes described in the Qu *et al.* (2024), with prior
500 error covariance \mathbf{S}_A , given as a diagonal matrix with values of 0.5 (squared). The \mathbf{I} is the identity
501 matrix. The prior covariances for each emission category (livestock, waste, rice, coal, oil and
502 gas, and fires) are described in Worden et al. (2022) and Worden et al. (2023).

503

504

505 ***Uncertainty Calculation***

506

507 After projecting the estimate for integrated fluxes at 5x4 degrees (\mathbf{x}) to emissions by sector at
 508 1x1 degree (\mathbf{z}), we can describe \mathbf{z} using Equation 2 with corresponding averaging kernel as
 509 discussed in the introduction (and now including uncertainties):

$$511 \mathbf{z} = \mathbf{z}_A + \mathbf{A}(\mathbf{z} - \mathbf{z}_A) + \boldsymbol{\delta}_n + \boldsymbol{\delta}_m \quad (7)$$

512
 513 where $\boldsymbol{\delta}_n$ and $\boldsymbol{\delta}_m$ are the errors from measurement error and model error respectively. The
 514 measurement and model errors are discussed in Worden *et al.* (2022, 2023). The error
 515 covariance for \mathbf{z} is then given by:

$$517 E\|\mathbf{z} - \mathbf{z}\| = \mathbf{Z}_{\text{total}} = (\mathbf{I} - \mathbf{A})\mathbf{Z}_A(\mathbf{I} - \mathbf{A})^T + \mathbf{S}_n + \mathbf{S}_m \quad (8)$$

518
 519 Note that the inverse of the Hessian (Equation 6) is equivalent to the first two terms (Worden *et al.*
 520 *et al.* 2004; Bowman *et al.* 2006):

$$522 \mathbf{Z} = (\mathbf{I} - \mathbf{A})\mathbf{Z}_A(\mathbf{I} - \mathbf{A})^T + \mathbf{S}_n \quad (9)$$

523
 524 Equation 9 allows us to separate the “smoothing error” (the first term on the RHS of Equation 9),
 525 from the measurement error in order to better evaluate comparisons between the GOSAT and
 526 inventory methane estimates as discussed in the next section.

527
 528 In order to calculate the emissions for either a region (e.g. USA) or a category of emissions (e.g.
 529 rice), we must first sum the corresponding elements of the state vector:

$$532 \mathbf{z}_i = \mathbf{h}_i \mathbf{z}, \quad (10)$$

533
 534 Where \mathbf{h}_i is a column vector that projects the desired elements of \mathbf{z} to region or sector i , \mathbf{z}_i . As
 535 discussed in Worden *et al.* (2022), the uncertainty of \mathbf{z}_i is then given by

$$537 \sigma_i^2 = \mathbf{h}_i \mathbf{Z}_{\text{total}} \mathbf{h}_i^T \quad (11)$$

538

539

540 As discussed in these previous papers, this uncertainty calculation accounts for the effects of
541 cross-terms (e.g. wetlands, OH, fires). Equation (11) is what is used to calculate the
542 uncertainties shown in the figures and the tables in this paper.

543

544 **Appendix B: Bayesian / Optimal Estimation Approach for Comparing Inventory to top-** 545 **down Inversion**

546 To compare a $0.1^\circ \times 0.1^\circ$ inventory with top-down fluxes based on an inversion of atmospheric
547 data, we first project the inventory to the same spatial scale as the top-down fluxes and then
548 account for the sensitivity of the top-down estimates. The native resolution of the gridded
549 inventories is 0.1° , provided by sector. In contrast, the GOSAT based fluxes are at a coarser
550 resolution of $5^\circ \times 4^\circ$ (longitude \times latitude) and represent integrated fluxes (Qu et al., 2024) with
551 no sectoral specificity in each grid. Our approach is to first re-grid the inventory to $1^\circ \times 1^\circ$, while
552 retaining sectoral distinctions (e.g., livestock, waste, rice, coal, oil & gas). As discussed in the
553 following paragraph, we then project the $5^\circ \times 4^\circ$ GOSAT-inverted methane fluxes to sector-
554 specific emissions at $1^\circ \times 1^\circ$ resolution as discussed in Appendix A. We selected this
555 intermediate resolution to better represent national emission patterns, as a $5^\circ \times 4^\circ$ grid can cause
556 significant overlapping flux contributions from neighboring countries such as the United States,
557 Canada, and Mexico.

558

559 The comparison approach is described in Worden *et al.* (2023) and summarized here. We next
560 project the inventory (\mathbf{z}_i) through the “inversion operator” (Equation 2) in order to account for
561 the choice of a priori in the inversion and the sensitivity of the emissions (Rodgers 2000, Worden
562 et al. 2022, 2023).

563

$$564 \mathbf{z}_i = \mathbf{z}_A + \mathbf{A}(\mathbf{z}_i - \mathbf{z}_A) \quad (12)$$

565

566 Where \mathbf{z}_A is a vector describing the *a priori* methane emissions used for the top-down estimate
567 and \mathbf{A} is the averaging kernel matrix calculated for that inversion. The averaging kernel matrix is
568 a function of the prior and posterior covariance, \mathbf{Z} and \mathbf{Z}_A :

$$569 \mathbf{A} = \mathbf{I} - \mathbf{Z}\mathbf{Z}_A^{-1} \quad (13)$$

570
571 The DOFS shown in Table 1 are calculated by taking the sum of diagonal elements (or trace) of
572 the averaging kernel corresponding to the sector.

573
574 After application of the inversion operator a comparison of these modified inventory emissions
575 with the GOSAT- based emissions (Cusworth et al. 2021, Worden et al. 2023, Appendix A) is
576 given by:

$$577 \mathbf{z} - \mathbf{z}_i = \mathbf{A}(\boldsymbol{\delta}_i) + \boldsymbol{\delta}_n + \boldsymbol{\delta}_m \quad (14)$$

578
579 Where $\boldsymbol{\delta}_i$ is the uncertainty in the inventory, $\boldsymbol{\delta}_n$ is the uncertainty in the inversely estimated
580 emissions due to noise in the atmospheric data, and $\boldsymbol{\delta}_m$ is the uncertainty in the model used to
581 project concentrations to emissions. The effect of the prior, \mathbf{z}_A , is also removed in this
582 comparison described by Equation 14 so that the inventory can be compared to the satellite based
583 emissions without this large effect of smoothing error on the comparison (see subsequent figures
584 and supplemental). The error of the difference between satellite estimate and this adjusted
585 inventory is then the expectation of the difference:

$$586 E\|\mathbf{z} - \mathbf{z}_i\| = \mathbf{A}\mathbf{S}_i\mathbf{A}^T + \mathbf{S}_n + \mathbf{S}_m \quad (15)$$

587
588 Where \mathbf{S}_i is the covariance for the inventory uncertainties $\boldsymbol{\delta}_i$, \mathbf{S}_n is the measurement error
589 projected to emissions, and \mathbf{S}_m is the model error. Note that \mathbf{S}_n is directly calculated from the
590 inversion (Worden et al. 2023). The final term in Equation 15, the model error, can be highly
591 challenging to quantify. Previous studies have pointed towards the vertical mixing in models as
592 being the largest source of model error; too much or too little methane (or other trace gas) at the

597 surface as a result of incorrect mixing leads to inaccurate surface flux calculations (e.g. Jiang et
 598 al. 2013; Schuh et al. 2019; McNorton et al. 2020). These studies show that this effect is largest
 599 in the tropics where there is significant convection with an uncertainty that is about the same size
 600 as the data uncertainty. On the other hand, the mid-latitudes likely have smaller uncertainties of
 601 this type because of smaller uncertainties related to vertical mixing. For the purpose of this study
 602 we assume the model error is the same magnitude as the observation error S_n ; however continued
 603 advances are needed in both quantifying and mitigating this term, and how it affects the
 604 emissions estimates, in order to improve confidence in the comparisons between inventories and
 605 satellite data.

606 Note that if the GOSAT-based emissions are directly compared to the inventory without
 607 first passing the inventory through the inversion operator, then the uncertainties in the
 608 comparison are much larger and less meaningful as they include both the smoothing error of the
 609 data and the full uncertainty of the inventory:

$$610 \quad E\|\mathbf{z} - \mathbf{z}_i\| = \mathbf{S}_i + \mathbf{S}_n + \mathbf{S}_m + (\mathbf{I}-\mathbf{A})\mathbf{S}_\lambda(\mathbf{I}-\mathbf{A})^T \quad (16)$$

612
 613
 614 As a demonstration, we compare the GOSAT based emissions to the inventories both directly
 615 (uncertainties from Equation 16) and after applying the inversion operator (e.g. see Figures 2-4).

616
 617 **Use of Prior Swapping to evaluate emissions:** Equation 3 represents an alternative but
 618 equivalent approach for mitigating smoothing error when comparing atmospheric based
 619 emissions estimates to an inventory. After “swapping” the prior used for the GOSAT based
 620 emissions estimate with the inventory the new estimate has the following form:

$$621 \quad \mathbf{z}_{\text{GOSAT_New}} = \mathbf{z}_I + \mathbf{A}(\mathbf{z}_{\text{True}} - \mathbf{z}_I) + \boldsymbol{\delta}_n + \boldsymbol{\delta}_m \quad (17)$$

622
 623
 624 In this instance we want to take the expectation of the difference of $\mathbf{z}_{\text{GOSAT_New}}$ and \mathbf{z}_I as
 625 Equation (3) is equivalent to using \mathbf{z}_I as the *a priori* in the inversion described by Equation 1:

$$626 \quad \mathbf{z}_{\text{GOSAT_New}} - \mathbf{z}_I = \mathbf{A}(\mathbf{z}_{\text{True}} - \mathbf{z}_I) = \mathbf{A}(\boldsymbol{\delta}_I) + \boldsymbol{\delta}_n + \boldsymbol{\delta}_m \quad (18)$$

628
629 Equation 18 is the same as Equation 14 which demonstrates that the covariances as described by
630 Equation 15 (and hence uncertainties) are the same using prior swapping or an inversion operator
631 approach.

632
633

634 **Appendix C: Description of Inventories**

635
636

637 **(EPA GHGI)** The U.S. Environmental Protection Agency's (EPA) Inventory of U.S.
638 Greenhouse Gas Emissions and Sinks (GHGI) provides annual estimates of methane emissions
639 from anthropogenic sources. The gridded inventory used here covers emissions from sectors
640 such as agriculture, energy, waste, and coal for the years 2012 to 2018 (Maasakkers et al. 2023).

641 [Desai et al. \(2026\) provides updated national-scale inventory estimates for 1990–2024 that are](#)
642 [methodologically consistent with the EPA GHGI, allowing a comparable gridded product to be](#)
643 [developed and evaluated against satellite-based inversions using the benchmark framework](#)
644 [applied here.](#)

Formatted: Font: Times New Roman, 12 pt

Deleted: ¶

645 1. **Total Methane Emissions:** Gridded GHGI reports U.S. CONUS methane
646 emissions in 2015 at **23.7 Tg** of CH₄, which accounts for approximately **7% of global**
647 **anthropogenic methane emissions.**

648 2. **Sectoral Breakdown:** The Gridded GHGI includes methane emissions of 26
649 individual sectors. The largest sources are (see Table 2):

- 650 ○ **Livestock and Rice:** Emissions from enteric fermentation and manure
651 management constitute a significant portion of methane emissions from this sector
652 (8.8), with total agricultural emissions reaching **9.4 Tg** in 2018.
- 653 ○ **Oil and Gas:** Methane emissions from the oil and gas sectors, including
654 production & exploration, refining, transmission & storage, processing, and
655 distribution, account for approximately **6.9 Tg**.

- 657 ○ **Waste:** Emissions from municipal solid waste (MSW) landfills, industrial
658 landfills, wastewater treatment, and composting contributed to about **4.8 Tg**.
659 ○ **Coal Mines:** Methane from coal mining, including both active and abandoned
660 mines, contributed approximately **2.5 Tg**.

661 3. **Methodology:** The GHGI combines activity data with emission factors to
662 estimate methane emissions. The inventory uses data from sources such as the EPA’s
663 Greenhouse Gas Reporting Program (GHGRP) and U.S. Department of Agriculture
664 (USDA). The gridded GHGI uses facility-level data as well as proxy data for sources
665 with limited spatial information. to spatially and temporally disaggregate emissions

666 4. **Uncertainty and Adjustments:** The uncertainty in methane emissions is
667 accounted for with confidence intervals provided in the GHGI report. Recent updates to
668 the GHGI methodology include the inclusion of large well blowouts and emissions from
669 abandoned oil and gas wells, which had not been considered in previous iterations. The
670 inventory is continuously updated to reduce uncertainties and improve accuracy.

671 5. **Comparisons with Atmospheric Data:** The Gridded GHGI serves as a critical
672 input for atmospheric inversions and can be compared with top-down estimates from
673 satellite-based data, such as those from GOSAT.

Formatted: Indent: Left: 0.5", Space Before: 12 pt, After: 12 pt

Deleted: ¶

674 **(EDGAR 2024)** The Emissions Database for Global Atmospheric Research

675
676 The EDGAR series of inventories provides gridded (0.1x0.1 degree) emissions of the key
677 anthropogenic emissions contributing to the global methane budget. We refer the reader to
678 Crippa et al. (2020, 2024) for a description of this inventory. Emissions are generated by
679 downscaling national totals by sector using spatial proxies and projected to the 0.1 x 0.1 grid. In
680 order to improve the accuracy of comparisons between the EDGAR inventory and the GOSAT-
681 based fluxes, we regrid their sub-categories to livestock, waste, coal, gas, oil, and rice (e.g. see
682 Figure 1 for the EDGAR 2024 oil&gas emissions).
683

686 **(NOAA FOG)** The NOAA fuel-based oil and gas (FOG) inventory provides oil and gas
687 emissions for the contiguous United States (CONUS) gridded at 4km x 4km and are then
688 regridded to (0.1 x 0.1 degree) for this work (Francoeur et al. 2021). The NOAA FOG methane
689 emissions inventory is generated through a hybrid approach that combines activity data with
690 atmospheric measurements to provide a more comprehensive and accurate assessment of
691 methane emissions from the oil and gas sector. FOG combines combustion activity of drilling
692 and production engines with fuel-based nitrogen oxides (NO_x) emission factors from
693 measurements and empirical models (Gorchov-Negron *et al.* 2018). The activity-based NO_x
694 emissions have been evaluated with airborne NOAA WP-3 measurements over a comprehensive
695 number of US oil and gas basins during the Southeast Nexus Study
696 (<https://csl.noaa.gov/projects/senex/>) and Shale Oil and Natural Gas Nexus Study
697 (<https://csl.noaa.gov/projects/songnex/>), as well as with spaceborne observations (Dix *et al.*
698 2020, 2022). Oil and gas methane emissions are then inferred by tracer-tracer ratios observed by
699 the aircraft relative to NO_x analyzed for each oil and gas basin measured (Francoeur *et al.* 2021).
700 The hybrid approach in principle allows for a better representation of emissions compared to
701 traditional activity-based inventories as the atmospheric data likely better captures the effect of
702 **fugitive emissions** and other hard-to-measure sources that are often underrepresented in other
703 activity based inventory methods. Additionally, atmospheric measurements help to address
704 uncertainties by cross-referencing emission estimates with observed methane concentrations,
705 thus improving the overall reliability of the inventory.

706 Key findings from the FOG inventory include:

- 707 1. **Methane Emissions:** The FOG inventory estimates total methane emissions from
708 oil and natural gas production **at 14.1 ± 2.0 Tg CH₄/yr for 2015.**
- 709 2. **Sectoral Breakdown:** The FOG inventory includes methane emissions from
710 drilling, production, gathering, and processing activities. The contribution of methane
711 emissions from the production and drilling phases is particularly significant, comprising
712 about **60% of total methane emissions** during the oil and gas production process.
- 713 3. **Uncertainty and Evaluation:** The methane estimates from the FOG inventory
714 are supported by aircraft-derived "top-down" emission measurements, which help

715 validate the inventory's accuracy. Uncertainties are evaluated through a Monte-Carlo
716 analysis of the NO_x emissions and emissions factors (Francoeur *et al.* 2021)

717

718 **Code Availability**

719 The code for the sectoral attribution is available here (Worden and Pandey 2025):

720 <https://doi.org/10.5281/zenodo.15786798>].

721 A Python notebook demonstrating the benchmarking approach with the GOSAT inversion fluxes
722 is available at Pandey, S., & Worden, J. (2025). Evaluation of Methane Emissions Inventory
723 Using Satellite Flux Inversions Data set <https://doi.org/10.5281/zenodo.16921536> (Pandey and
724 Worden 2025)

725

726 **Data Availability**

727 GOSAT-based fluxes and emissions by sector are also available on Zenodo:

728 <https://zenodo.org/records/15786798>. (Worden and Pandey 2025)

729

730 **Author Contributions**

731 JW designed the study, performed sectoral attribution, and wrote the paper draft SP performed
732 the inventory comparison analysis, made the figures and supported the paper writing. HN, JDM,
733 and KB supported the analysis and paper writing. CH and CL supported the FOG analysis. DG
734 and LS supported interpretation of the inventories. DJ, LE, DV, JE, and ZQ produced the
735 GOSAT fluxes, supported the interpretation, and reviewed the paper.

736

737 **Competing Interests: The authors declare that to their knowledge there are no competing**
738 **interests.**

739

740 **Acknowledgements**

741

742 Part of this research was carried out at the Jet Propulsion Laboratory, California Institute of
743 Technology, under a contract with the National Aeronautics and Space Administration. Chatgpt
744 used to support paper editing.

745

746 **Financial Support**

747

748 This work is funded by the NASA Carbon Monitoring System (Carbon Monitoring System
749 NNH23ZDA001N-CMS) and through the NASA Greenhouse Gas Center.

750 **References**

751

752 Alvarez, R. A., Zavala-Araiza, D., Lyon, D. R., Allen, D. T., Barkley, Z. R., Brandt, A. R., et al.
753 (2018). Assessment of methane emissions from the U.S. oil and gas supply chain. *Science*,
754 361(6398), eaar7204. <https://doi.org/10.1126/science.aar7204>

755 Barkley, Z. R., Lauvaux, T., Davis, K. J., Miles, N. L., Richardson, S. J., Jacobson, G., et al.
756 (2022). Estimating methane emissions from the Marcellus and Delaware Basins using continuous
757 tower observations. *Atmospheric Chemistry and Physics*, 23, 6127–6145.
758 <https://doi.org/10.5194/acp-23-6127-2023>

759 Bowman, K. W., Rodgers, C. D., Kulawik, S. S., Worden, J., Sarkissian, E., Osterman, G., Steck,
760 T., Lou, M., Eldering, A., Shephard, M., Worden, H., Lampel, M., Clough, S., Brown, P.,
761 Rinsland, C., Gunson, M., and Beer, R.: Tropospheric Emission Spectrometer: Retrieval Method
762 and Error Analysis, *Ieee T Geosci Remote*, 44, 1297–1307,
763 <https://doi.org/10.1109/tgrs.2006.871234>, 2006.

764 Crippa, M., Solazzo, E., Huang, G., Guizzardi, D., Koffi, E., Muntean, M., et al. (2020). High
765 resolution temporal profiles in the Emissions Database for Global Atmospheric Research.
766 *Scientific Data*, 7, 121. <https://doi.org/10.1038/s41597-020-0462-2>

767 Crippa, M., Guizzardi, D., Pagani, F., Schiavina, M., Melchiorri, M., Pisoni, E., et al. (2024).
768 Insights into the spatial distribution of global, national, and subnational greenhouse gas
769 emissions in the Emissions Database for Global Atmospheric Research (EDGAR v8.0). *Earth*
770 *System Science Data*, 16(6), 2811–2830. <https://doi.org/10.5194/essd-16-2811-2024>

771 Crippa, M., Guizzardi, D., Pagani, F., Banja, M., Muntean, M., Schaaf, E., Monforti-Ferrario, F.,
772 Becker, W., Quadrelli, R., Risquez Martin, A., Taghavi-Moharamli, P., Köykkä, J., Grassi, G.,
773 Rossi, S., Melo, J., Oom, D., Branco, A., San-Miguel, J., Manca, G., Pisoni, E., Vignati, E. and
774 Pekar, F., GHG emissions of all world countries, Publications Office of the European Union,
775 Luxembourg, 2024, doi:10.2760/4002897, JRC138862

776

777 Cusworth, D. H., Bloom, A. A., Ma, S., Miller, C. E., Bowman, K., Yin, Y., et al. (2021). A
778 Bayesian framework for deriving sector-based methane emissions from top-down fluxes.
779 *Communications Earth & Environment*, 2, 242. <https://doi.org/10.1038/s43247-021-00312-6>

780 Cusworth, D. H., Duren, R. M., Ayasse, A. K., Jiorle, R., Howell, K., Aubrey, A., et al. (2024).
781 Quantifying methane emissions from United States landfills. *Science*, 383(6690), 1499–1504.
782 <https://doi.org/10.1126/science.adi7735>

783 Cusworth, D. H., Duren, R. M., Thorpe, A. K., Tseng, E., Thompson, D., Guha, A., et al. (2020).
784 Using remote sensing to detect, validate, and quantify methane emissions from California solid
785 waste operations. *Environmental Research Letters*, 15, 054012. [https://doi.org/10.1088/1748-](https://doi.org/10.1088/1748-9326/ab7b99)
786 [9326/ab7b99](https://doi.org/10.1088/1748-9326/ab7b99)

787 Cusworth, D. H., Thorpe, A. K., Ayasse, A. K., Stepp, D., Heckler, J., Asner, G. P., et al. (2022).
788 Strong methane point sources contribute a disproportionate fraction of total emissions across
789 multiple basins in the United States. *Proceedings of the National Academy of Sciences*, 119,
790 e2202338119. <https://doi.org/10.1073/pnas.2202338119>

791 Desai, M., Camobreco, V., Hedger, T., Irving, W., Rewcastle, K., Steller, J., Barbieri,
792 L., Weitz, M., Murumkar, T., Fawcett, A., Lou, J., Cui, R., and Hultman, N.: *Greenhouse*
793 *Gas Inventory and Analysis for the United States: 1990–2024*, Center for Global
794 Sustainability, University of Maryland, College Park, 2026.

795 Dix, B., Francoeur, C., Li, M., Serrano-Calvo, R., Levelt, P. F., Veeffkind, J. P., McDonald, B.
796 C., and de Gouw, J. A.: Quantifying NO_x emissions from U.S. oil and gas production regions
797 using TROPOMI NO₂, *ACS Earth Space Chem.*, **6**(2), 403-414,
798 <https://doi.org/10.1021/acsearthspacechem.1c00387>, 2022.
799

800 Dix, B., Bruin, J., Roosenbrand, E., Vlemmix, T., Francoeur, C., Gorchov-Negron, A. M.,
801 McDonald, B., Zhizhin, M., Elvidge, C., Veeffkind, P., Levelt, P., and de Gouw, J. A.: Nitrogen
802 oxide emissions from U.S. oil and gas production: Recent trends and source
803 attribution, *Geophys. Res. Lett.*, **47**(1), e2019GL085866, <https://doi.org/10.1029/2019GL085866>,
804 2020.
805

806 East, J. D., Jacob, D. J., Jervis, D., Balasus, N., Estrada, L. A., Hancock, S. E., Sulprizio, M. P.,
807 Thomas, J., Wang, X., Chen, Z., Varon, D. J., and Worden, J. R.: Worldwide inference of
808 national methane emissions by inversion of satellite observations with UNFCCC prior estimates,
809 *Nat. Commun.*, **16**, 11004, <https://doi.org/10.1038/s41467-025-67122-8>, 2025.

810 EDGAR (Emissions Database for Global Atmospheric Research) Community GHG Database, a
811 collaboration between the European Commission, Joint Research Centre (JRC), the International
812 Energy Agency (IEA), and comprising IEA-EDGAR CO₂, EDGAR CH₄, EDGAR N₂O,
813 EDGAR F-GASES version 2024 European Commission, JRC (Datasets).
814 https://edgar.jrc.ec.europa.eu/dataset_ghg2024 (accessed: 1 October 2025)

815

816 [EPA \(U.S. Environmental Protection Agency\). \(2011\). Fact Sheet on Mandatory Reporting of](https://www.epa.gov/sites/default/files/2015-07/documents/part98factsheet.pdf)
817 [Greenhouse Gases \(40 CFR part 98\). \[https://www.epa.gov/sites/default/files/2015-\]\(https://www.epa.gov/sites/default/files/2015-07/documents/part98factsheet.pdf\)](https://www.epa.gov/sites/default/files/2015-07/documents/part98factsheet.pdf)
818 [07/documents/part98factsheet.pdf](https://www.epa.gov/sites/default/files/2015-07/documents/part98factsheet.pdf)

819 Etiope, G., Ciotoli, G., Schwietzke, S., & Schoell, M. (2018). Gridded maps of geological
820 methane emissions and their isotopic signature. *Earth System Science Data*, **11**, 1–22.
821 <https://doi.org/10.5194/essd-11-1-2019>

822 Francoeur, C. B., McDonald, B. C., Gilman, J. B., Zarzana, K. J., Dix, B., Brown, S. S., et al.
823 (2021). Quantifying methane and ozone precursor emissions from oil and gas production regions
824 across the contiguous US. *Environmental Science & Technology*, 55(13), 9129–9139.
825 <https://doi.org/10.1021/acs.est.0c07352>

826 Gorchoy Negron, A. M., McDonald, B. C., McKeen, S. A., Peischl, J., Ahmadov, R., de Gouw,
827 J. A., Frost, G. J., Hastings, M. G., Pollack, I. B., Ryerson, T. B., Thompson, C., Warneke, C.,
828 and Trainer, M.: Development of a fuel-based oil and gas inventory of nitrogen oxides
829 emissions, *Environ. Sci. Technol.*, **52**, 10175–10185, <https://doi.org/10.1021/acs.est.8b02245>,
830 2018.

831 [Gordon, D. No Standard Oil: Managing Abundant Petroleum in a Warming World \(paperback
832 edition\). Oxford University Press, 2025. \[https://global.oup.com/academic/product/no-standard-
833 oil-9780197832165?cc=us&lang=en&\]\(https://global.oup.com/academic/product/no-standard-oil-9780197832165?cc=us&lang=en&\)](https://doi.org/10.1021/acs.est.8b02245)

834 Hancock, S. E., Jacob, D., Chen, Z., Nesser, H., Davitt, A., Varon, D. J., et al. (2025). Satellite
835 quantification of methane emissions from South American countries: A high-resolution inversion
836 of TROPOMI and GOSAT observations. *Atmospheric Chemistry and Physics*, 25, 797–833.
837 <https://doi.org/10.5194/acp-25-797-2025>

838 Herman, R. L., Cherry, J. E., Young, J., Welker, J. M., Noone, D., Kulawik, S. S., & Worden, J.
839 (2014). Aircraft validation of Aura Tropospheric Emission Spectrometer retrievals of HDO /
840 H₂O. *Atmospheric Measurement Techniques*, 120(9), 3127–3138. [https://doi.org/10.5194/amt-7-
841 3127-2014](https://doi.org/10.5194/amt-7-3127-2014)

842

843 Hmiel, B., Petrenko, V. V., Dyonisius, M. N., Buizert, C., Smith, A. M., Place, P. F., et al.
844 (2020). Preindustrial 14CH₄ indicates greater anthropogenic fossil CH₄ emissions. *Nature*, 578,
845 409–412. <https://doi.org/10.1038/s41586-020-1991-8>

846 Hristov, A. N., Harper, M., Meinen, R., Day, R., Lopes, J., Ott, T., et al. (2017). Discrepancies
847 and uncertainties in bottom-up gridded inventories of livestock methane emissions for the
848 contiguous United States. *Environmental Science & Technology*, 51(23), 13668–13677.
849 <https://doi.org/10.1021/acs.est.7b03332>

850 [IEA \(International Energy Agency\). \(2025\). Global Methane Tracker 2025.](#)
851 <https://www.iea.org/reports/global-methane-tracker-2025/key-findings>

852 Jacob, D. J., Varon, D. J., Cusworth, D. H., Dennison, P. E., Frankenberg, C., Gautam, R., et al.
853 (2022). Quantifying methane emissions from the global scale down to point sources using
854 satellite observations of atmospheric methane. *Atmospheric Chemistry and Physics*, 22, 9617–
855 9646. <https://doi.org/10.5194/acp-22-9617-2022>

856 Janardanan, R., Maksyutov, S., Wang, F., Nayagam, L., Sahu, S. K., Mangaraj, P., et al. (2024).
857 Country-level methane emissions and their sectoral trends during 2009–2020 estimated by high-
858 resolution inversion of GOSAT and surface observations. *Environmental Research Letters*, 19,
859 034007. <https://doi.org/10.1088/1748-9326/ad2436>

860 Kruskamp, N., Lohman, H., Burnette, A., Coxen, C., Ellermeier, N., Bollenbacher, J., Powers, J.,
861 Coffield, S., Farhat, Y., and Maasackers, J.: *Gridded U.S. Anthropogenic Methane Greenhouse*
862 *Gas Inventory (gridded GHGI)*, Zenodo, <https://doi.org/10.5281/zenodo.16782735>, 2025.

863 Kort, E. A., Eluszkiewicz, J., Stephens, B. B., Miller, J. B., Gerbig, C., Nehr Korn, T., et al.
864 (2008). Emissions of CH₄ and N₂O over the United States and Canada based on a receptor-
865 oriented modeling framework and COBRA-NA atmospheric observations. *Geophysical*
866 *Research Letters*, 35, L18808. <https://doi.org/10.1029/2008GL034031>

867 Lu, X., Jacob, D. J., Zhang, Y., Shen, L., Sulprizio, M. P., Maasackers, J. D., et al. (2023).
868 Observation-derived 2010–2019 trends in methane emissions and intensities from U.S. oil and
869 gas fields tied to activity metrics. *Proceedings of the National Academy of Sciences*, 120,
870 e2217900120. <https://doi.org/10.1073/pnas.2217900120>

871 Maasackers, J. D., Jacob, D. J., Sulprizio, M. P., Scarpelli, T. R., Nesser, H., Sheng, J., et al.
872 (2021). 2010–2015 North American methane emissions, sectoral contributions, and trends: a
873 high-resolution inversion of GOSAT observations of atmospheric methane. *Atmospheric*
874 *Chemistry and Physics*, 21, 4339–4356. <https://doi.org/10.5194/acp-21-4339-2021>

875 Maasackers, J. D., McDuffie, E. E., Sulprizio, M. P., Chen, C., Schultz, M., Brunelle, L., et al.
876 (2023). A gridded inventory of annual 2012–2018 U.S. anthropogenic methane emissions.

877 *Environmental Science & Technology*, 57(43), 16276–16288.
878 <https://doi.org/10.1021/acs.est.3c05138>

879 Miller, S. M., Wofsy, S. C., Michalak, A. M., Kort, E. A., Andrews, A. E., Biraud, S. C., et al.
880 (2013). Anthropogenic emissions of methane in the United States. *Proceedings of the National*
881 *Academy of Sciences*, 110(50), 20018–20022. <https://doi.org/10.1073/pnas.1314392110>

882 Nesser, H., Jacob, D. J., Maasackers, J. D., Lorente, A., Chen, Z., Lu, X., et al. (2024). High-
883 resolution U.S. methane emissions inferred from an inversion of 2019 TROPOMI satellite data:
884 Contributions from individual states, urban areas, and landfills. *Atmospheric Chemistry and*
885 *Physics*, 24, 5069–5091. <https://doi.org/10.5194/acp-24-5069-2024>

886 Nisbet, E. G., Manning, M. R., Dlugokencky, E. J., Fisher, R. E., Lowry, D., Michel, S. E., et al.
887 (2019). Very strong atmospheric methane growth in the 4 years 2014–2017: Implications for the
888 Paris Agreement. *Global Biogeochemical Cycles*, 33, 318–342.
889 <https://doi.org/10.1029/2018GB006009>

890 Pandey, S., Worden, J., Cusworth, D. H., Varon, D. J., Thill, M. D., Jacob, D. J., and Bowman,
891 K. W.: Relating multi-scale plume detection and area estimates of methane emissions: a
892 theoretical and empirical analysis, *Environ. Sci. Technol.*, 59, 7931–7947,
893 <https://doi.org/10.1021/acs.est.4c07415>, 2025.

894 Pandey, S. and Worden, J.: *Evaluation of Methane Emissions Inventory Using Satellite Flux*
895 *Inversions* (data set), Zenodo, <https://doi.org/10.5281/zenodo.16921536>, 2025.

896 Parker, R., Boesch, H., Cogan, A., Fraser, A., Feng, L., Palmer, P. I., et al. (2011). Methane
897 observations from the Greenhouse Gases Observing SATellite: Comparison to ground-based
898 TCCON data and model calculations. *Geophysical Research Letters*, 38, L15807.
899 <https://doi.org/10.1029/2011GL047871>

900 Petrescu, A. M. R., Peters, G. P., Engelen, R., Houweling, S., Brunner, D., Tsuruta, A., et al.
901 (2024). Comparison of observation- and inventory-based methane emissions for eight large
902 global emitters. *Earth System Science Data*, 16, 4325–4350. [https://doi.org/10.5194/essd-16-](https://doi.org/10.5194/essd-16-4325-2024)
903 [4325-2024](https://doi.org/10.5194/essd-16-4325-2024)

904 Qu, Z., Jacob, D. J., Zhang, Y., Shen, L., Varon, D. J., Lu, X., Scarpelli, T., Bloom, A., Worden,
905 J., and Parker, R. J.: Attribution of the 2020 surge in atmospheric methane by inverse analysis of
906 GOSAT observations, *Environ Res Lett*, <https://doi.org/10.1088/1748-9326/ac8754>, 2022.

907 Qu, Z., Jacob, D. J., Bloom, A. A., Worden, J. R., Parker, R. J., & Boesch, H. (2024). Inverse
908 modeling of 2010–2022 satellite observations shows that inundation of the wet tropics drove the
909 2020–2022 methane surge. *Proceedings of the National Academy of Sciences*, 121,
910 e2402730121. <https://doi.org/10.1073/pnas.2402730121>

911 Rodgers, C. D., & Connor, B. J. (2003). Intercomparison of remote sounding instruments.
912 *Journal of Geophysical Research: Atmospheres*, 108, 4116.
913 <https://doi.org/10.1029/2002JD002299>

914 Saunois, M., Stavert, A. R., Poulter, B., Bousquet, P., Canadell, J. G., Jackson, R. B., et al.
915 (2020). The global methane budget 2000–2017. *Earth System Science Data*, 12, 1561–1623.
916 <https://doi.org/10.5194/essd-12-1561-2020>

917 Sherwin, E. D., Rutherford, J. S., Zhang, Z., Chen, Y., Wetherley, E. B., Yakovlev, P. V., et al.
918 (2024). U.S. oil and gas system emissions from nearly one million aerial site measurements.
919 *Nature*, 627, 328–334. <https://doi.org/10.1038/s41586-024-07117-5>

920 United States Environmental Protection Agency (EPA). (2023). Inventory of U.S. greenhouse
921 gas emissions and sinks: 1990–2021 (EPA 430-R-23-002). Retrieved from
922 <https://www.epa.gov/ghgemissions/inventory-us-greenhouse-gas-emissions-and-sinks>

923 Wecht, K. J., Jacob, D. J., & Sulprizio, M. P. (2014). Spatially resolving methane emissions in
924 California: constraints from the CalNex aircraft campaign and from present (GOSAT, TES) and
925 future (TROPOMI, *Atmospheric Chemistry and Physics*, 14(15). [https://doi.org/10.5194/acp-](https://doi.org/10.5194/acp-14-8173-2014)
926 14-8173-2014
927

928 Wolf, J., Asrar, G. R., & West, T. O. (2017). Revised methane emissions factors and spatially
929 distributed annual carbon fluxes for global livestock. *Carbon Balance and Management*, 12, 16.
930 <https://doi.org/10.1186/s13021-017-0084-y>

931 Worden, J., Kulawik, S., Shepard, M., Clough, S., Worden, H., Bowman, K., and Goldman, A.:
932 Predicted errors of tropospheric emission spectrometer nadir retrievals from spectral window
933 selection, *J Geophys Res Atmospheres* 1984 2012, 109, D09308,
934 <https://doi.org/10.1029/2004jd004522>, 2004.
935

936 Worden, J. R., Cusworth, D. H., Qu, Z., Yin, Y., Zhang, Y., Bloom, A. A., et al. (2022). The
937 2019 methane budget and uncertainties at 1° resolution and each country through Bayesian
938 integration of GOSAT total column methane data and a priori inventory estimates. *Atmospheric*
939 *Chemistry and Physics*, 22, 6811–6841. <https://doi.org/10.5194/acp-22-6811-2022>

940 Worden, J. R., Pandey, S., Zhang, Y., Cusworth, D. H., Qu, Z., Bloom, A. A., et al. (2023).
941 Verifying methane inventories and trends with atmospheric methane data. *AGU Advances*, 4.
942 <https://doi.org/10.1029/2023AV000871>

943 Worden, J. R. and Pandey, S.: *Evaluation of Methane Emissions Inventory Using Satellite Flux*
944 *Inversions*, Zenodo, <https://doi.org/10.5281/zenodo.15786798>, 2025.

945 [World Bank. \(2025\). Global Gas Flaring Tracker Report.](https://theodocs.worldbank.org/en/doc/bd2432bbb0e514986f382f61b14b2608-0400072025/original/Global-Gas-Flaring-Tracker-Report-July-2025.pdf)
946 [https://theodocs.worldbank.org/en/doc/bd2432bbb0e514986f382f61b14b2608-](https://theodocs.worldbank.org/en/doc/bd2432bbb0e514986f382f61b14b2608-0400072025/original/Global-Gas-Flaring-Tracker-Report-July-2025.pdf)
947 [0400072025/original/Global-Gas-Flaring-Tracker-Report-July-2025.pdf](https://theodocs.worldbank.org/en/doc/bd2432bbb0e514986f382f61b14b2608-0400072025/original/Global-Gas-Flaring-Tracker-Report-July-2025.pdf)

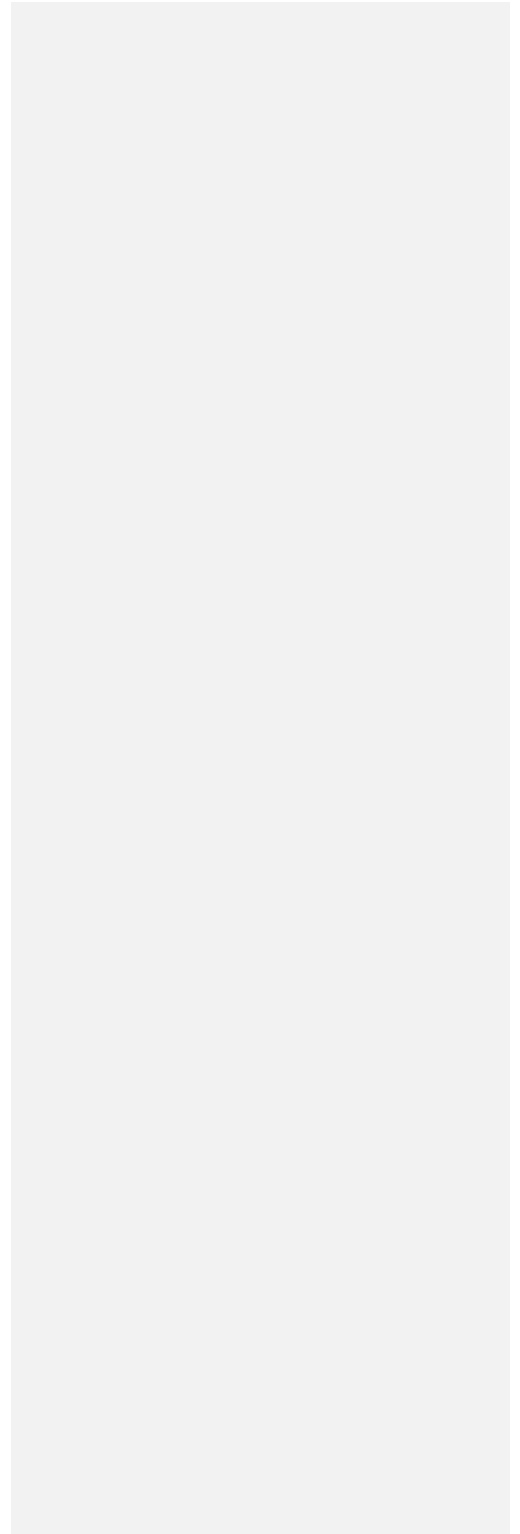
948 Zavala-Araiza, D., Lyon, D. R., Alvarez, R. A., Davis, K. J., Harriss, R., Herndon, S. C., et al.
949 (2015). Reconciling divergent estimates of oil and gas methane emissions. *Proceedings of the*
950 *National Academy of Sciences*, 112, 15597–15602. <https://doi.org/10.1073/pnas.1522126112>

951 Zhang, Y., Jacob, D. J., Lu, X., Maasakkers, J. D., Scarpelli, T. R., Sheng, J.-X., et al. (2021).
952 Attribution of the accelerating increase in atmospheric methane during 2010–2018 by inverse
953 analysis of GOSAT observations. *Atmospheric Chemistry and Physics*, 21, 3643–3666.
954 <https://doi.org/10.5194/acp-21-3643-2021>

955 Zhang, P., Zhang, Y., and Liang, R.: 2025: Correction of simulation biases in stratospheric
956 methane concentrations for the inverse analysis of satellite column observations, *J. Geophys.*
957 *Res.-Atmos.*, 30, <https://doi.org/10.1029/2024JD042596>.

958

959



960 [Figure Captions](#)

961

962 Figure 1: (Top Panels) Mean Emissions for Oil and Gas for 2015 (at 1x1 degree lon/lat gridding)
963 as calculated from the EPA, FOG, EDGAR inventories. (Bottom Panels) Differences between
964 FOG and EPA and EDGAR and EPA.

965

966 Figure 2: Comparison of the U.S. oil and gas (O&G) methane emissions in 2015 from the
967 GOSAT inversion with those from the FOG inventory. The upper left panel (a) shows the
968 GOSAT based estimate. The upper right panel (b) shows the original FOG emissions. The
969 middle left panel (c) shows the difference between the top two. The middle right panel shows the
970 difference between FOG emissions and GOSAT based emissions after applying the inversion
971 operator (denoted AK). All figures use 1x1 degree gridding; only differences larger than the
972 corresponding calculated uncertainty are shown. The bottom right panel (E) shows the diagonal
973 of the averaging kernel (or DOFS) corresponding to that location for oil and gas emissions.

974

975 Figure 3: Same as in Figure 2 but for the EDGAR inventory.

976

977 Figure 4: Same as in Figure 3 but for the EPA GHGI inventory.

978

979 **Figure 5:** Comparison of the integrated total oil and gas (O&G) emissions derived from GOSAT
980 with those from the FOG, EPA GHGI , and EDGAR 2024 inventories, both with and without the
981 inversion operator (AK) applied. Comparisons should be made between the GOSAT estimate
982 and the inventories with inversion operator (AK) applied.

983

984 **Figure 6:** Integrated totals for oil and gas emissions between 2012 and 2020. The GOSAT
985 inversion operator has been applied to the FOG, EPA GHGI , and EDGAR 2024 inventories; the
986 biases between the comparisons are therefore not due to the prior used with the GOSAT
987 inversion.

988 **Figure 7:** Similar to Figure 2 but for EDGAR 2024 livestock emissions

989

990 **Figure 8:** Similar to Figure 7 but for EPA GHGI livestock emissions

991

992 **Figure 9:** Comparison of the integrated livestock emissions derived from GOSAT with those
993 from the EPA GHGI and EDGAR 2024 inventories, both with and without the inversion
994 operator (AK) applied. Comparisons should be made between the GOSAT estimate and the
995 inventories with inversion operator (AK) applied.

996

997 **Figure 10:** Integrated totals for Livestock Emissions between 2012 and 2020. The inversion
998 operator has been applied to the inventories.

999

1000 **Figure 11:** Similar to Figure 2 but for EDGAR 2024 waste emissions

1001

1002 **Figure 12:** Similar to Figure 3 but for EPA GHGI waste emissions

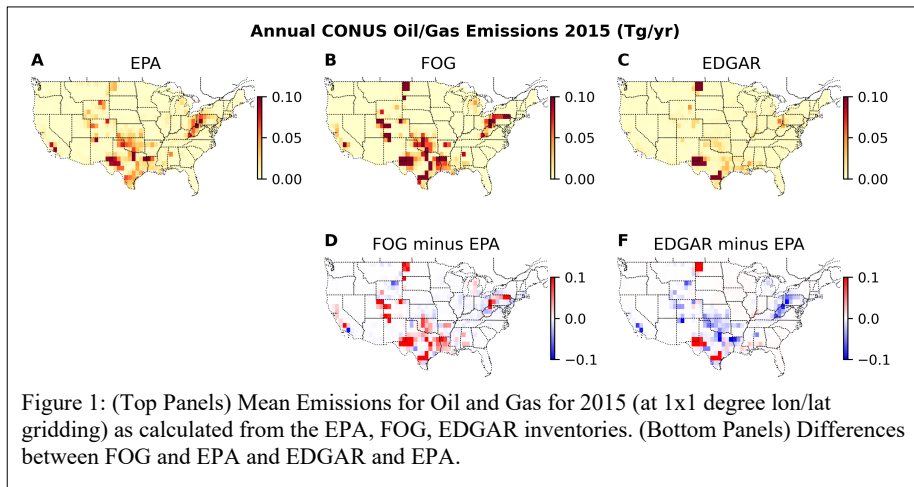
1003

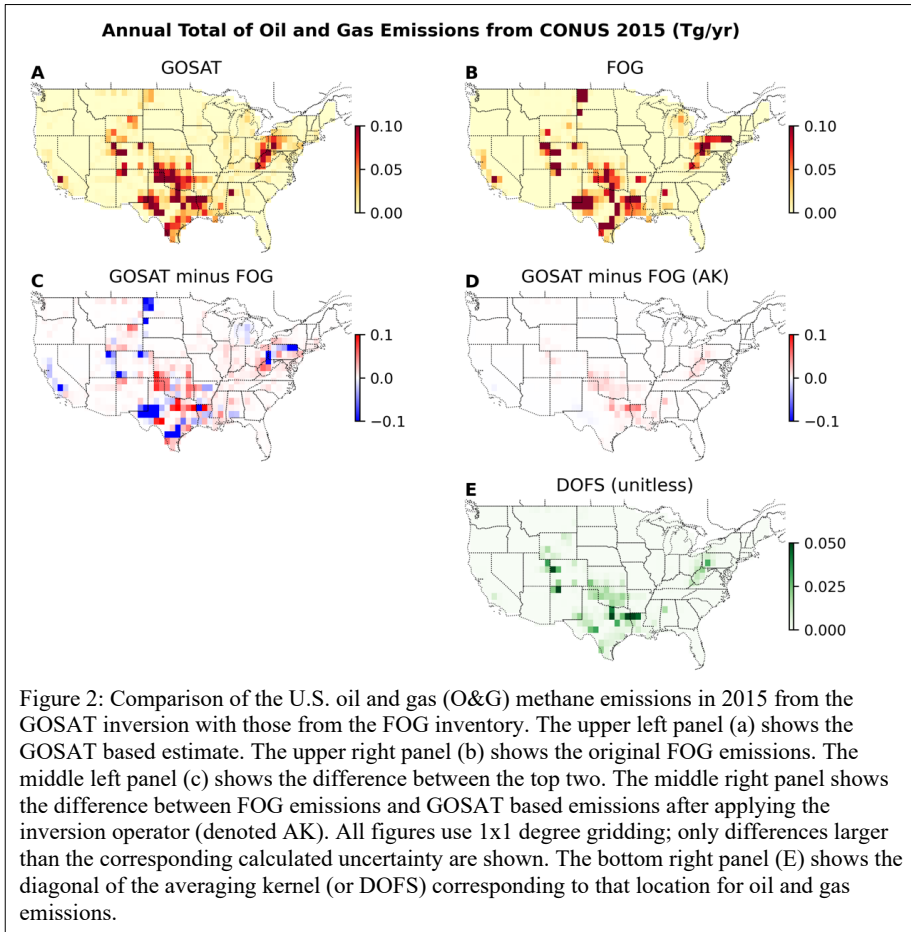
1004 **Figure 13:** Integrated total methane emissions from the waste sector based on GOSAT, along
1005 with estimates from the EPA GHGI and EDGAR 2024 inventories, both with and without the
1006 inversion operator applied.

1007

1008 [Figures](#)

1009





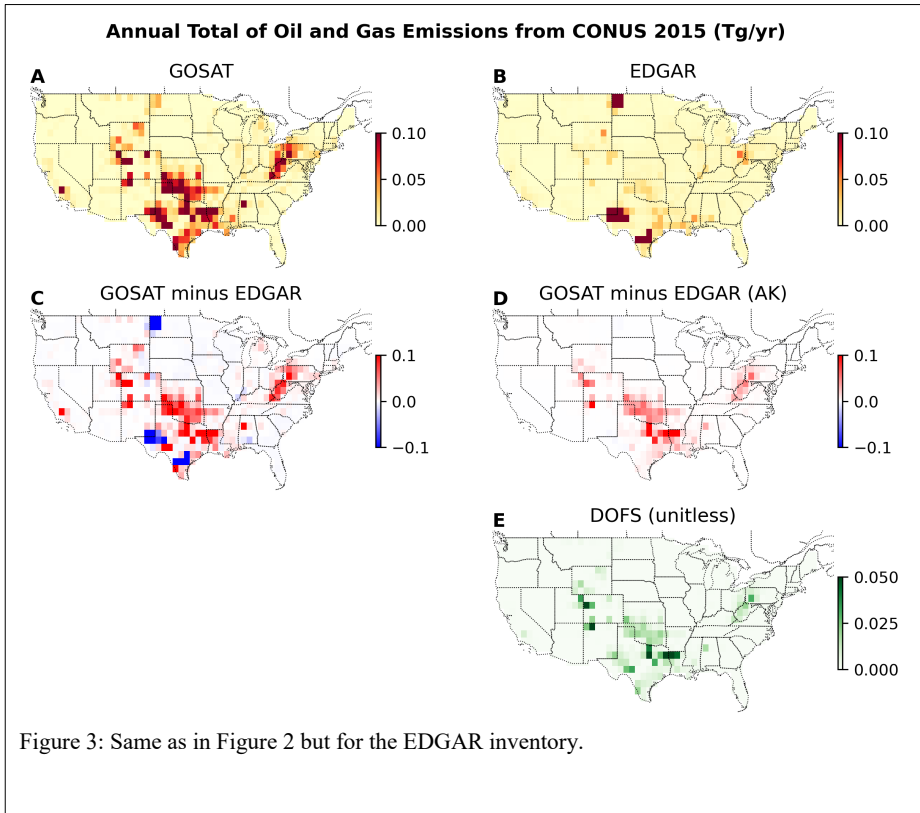
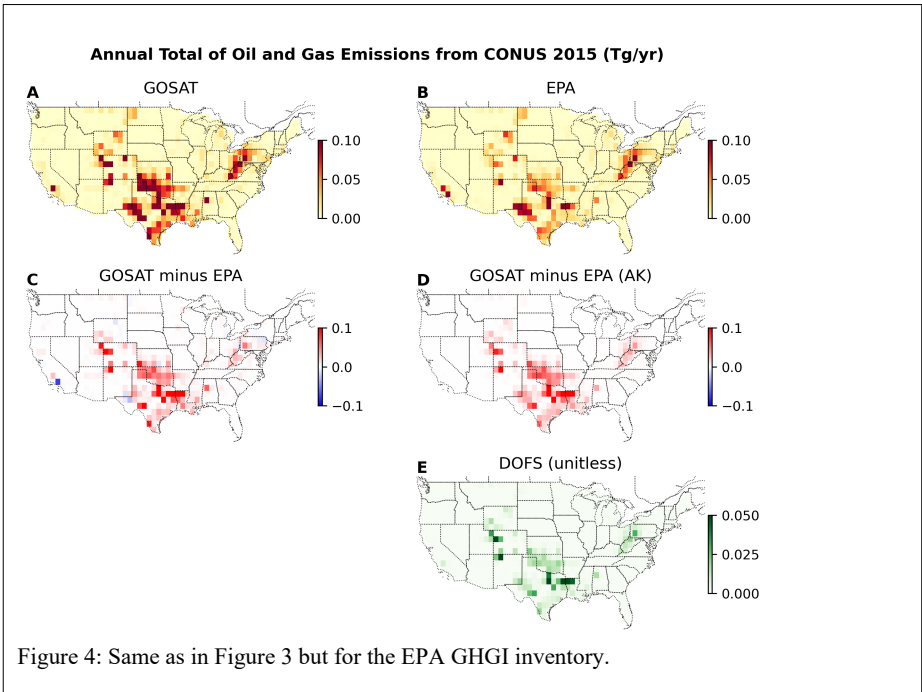
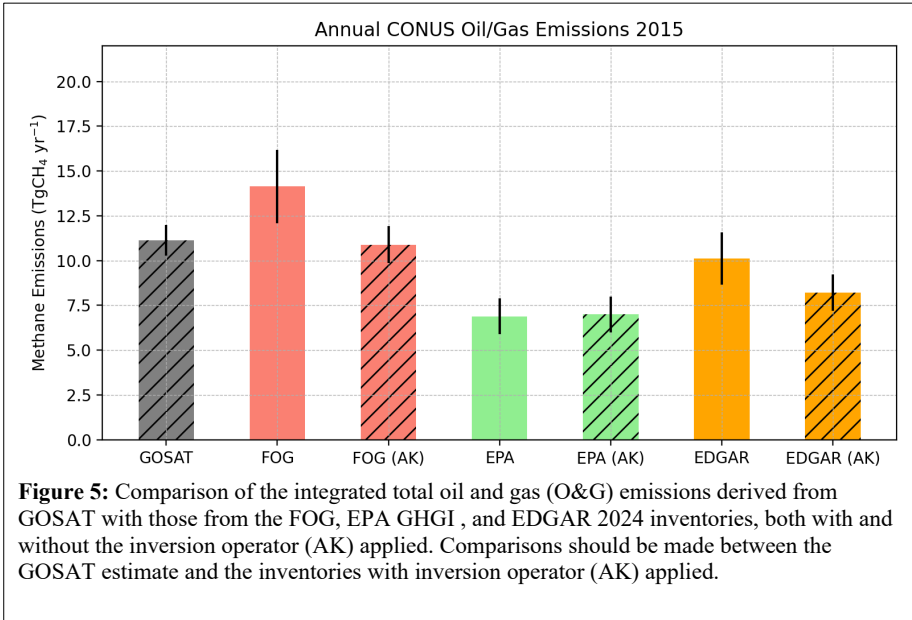


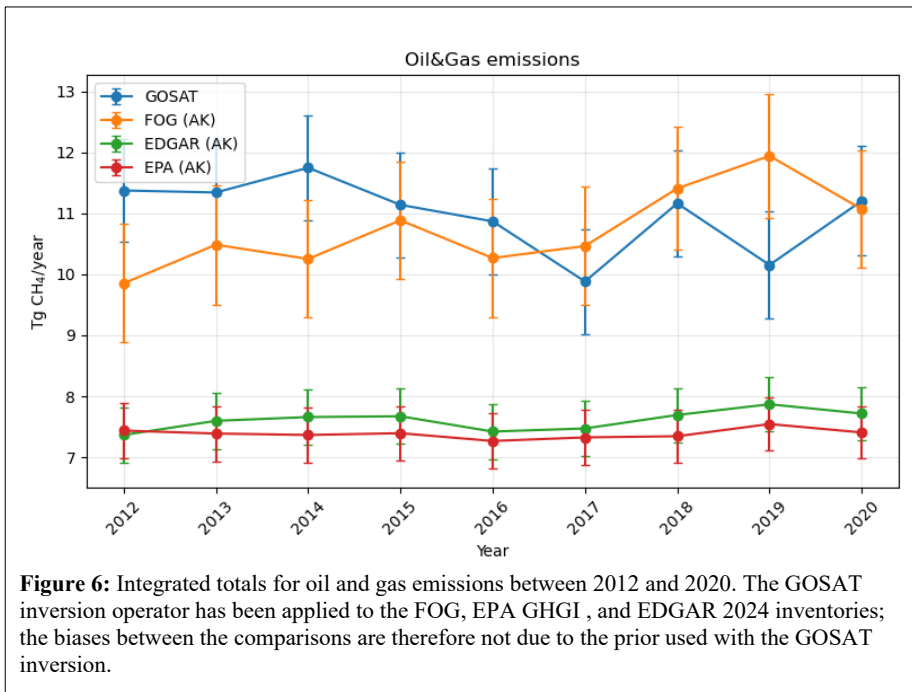
Figure 3: Same as in Figure 2 but for the EDGAR inventory.



1013
1014
1015
1016



1017
1018
1019



1020
1021
1022
1023

Figure 6: Integrated totals for oil and gas emissions between 2012 and 2020. The GOSAT inversion operator has been applied to the FOG, EPA GHGI, and EDGAR 2024 inventories; the biases between the comparisons are therefore not due to the prior used with the GOSAT inversion.

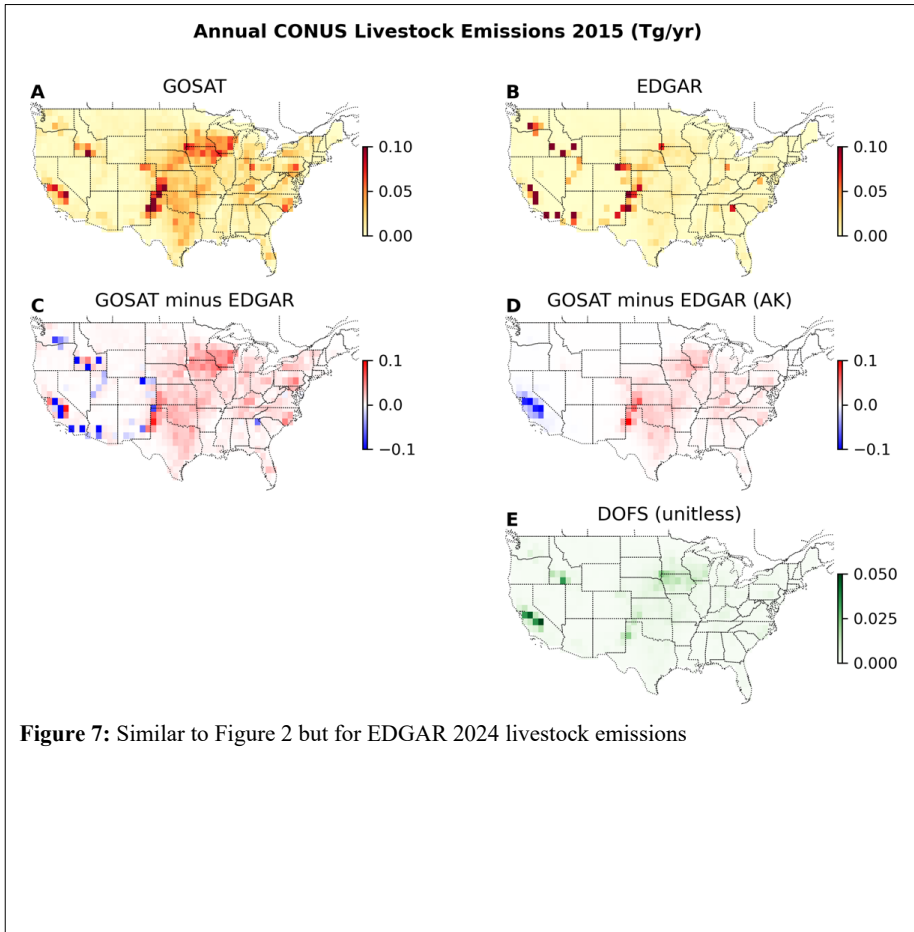


Figure 7: Similar to Figure 2 but for EDGAR 2024 livestock emissions

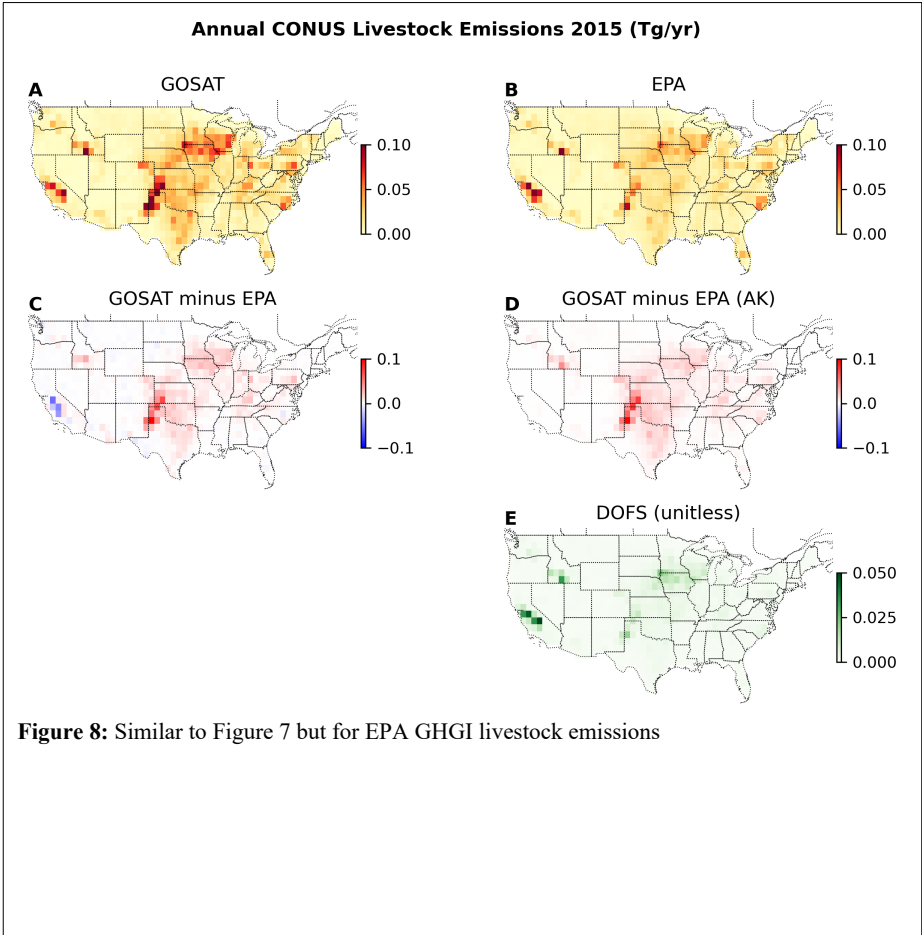
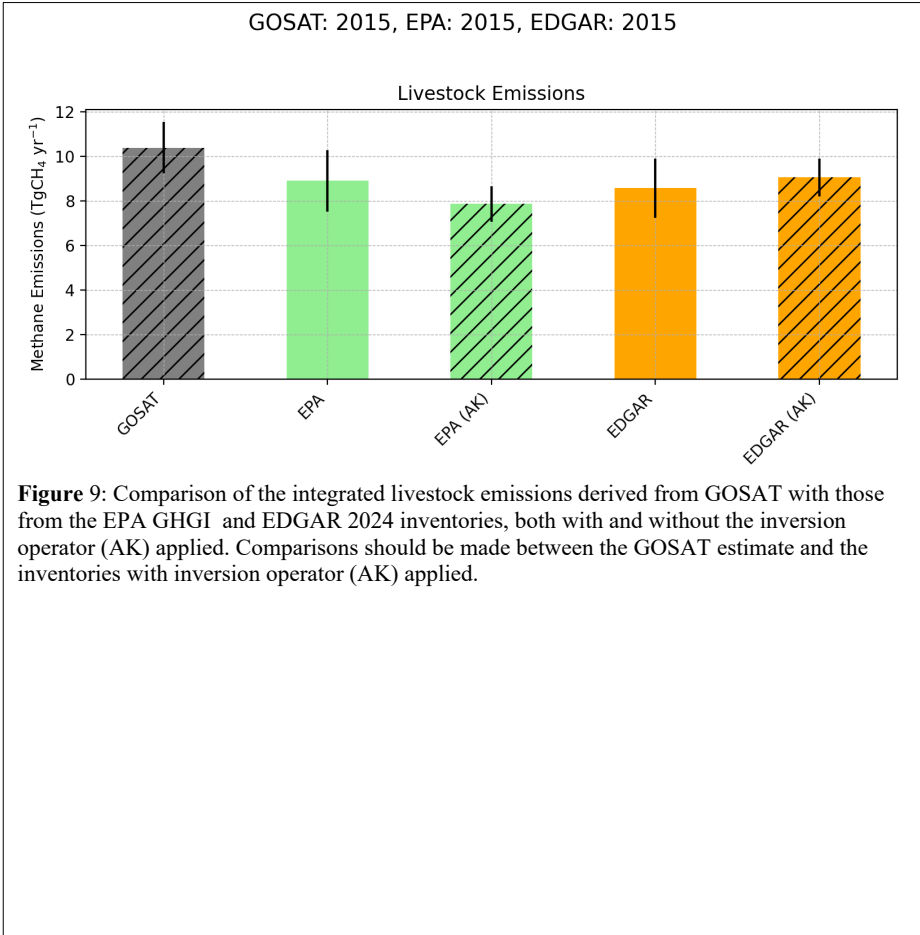


Figure 8: Similar to Figure 7 but for EPA GHGI livestock emissions



1027
1028
1029
1030
1031
1032

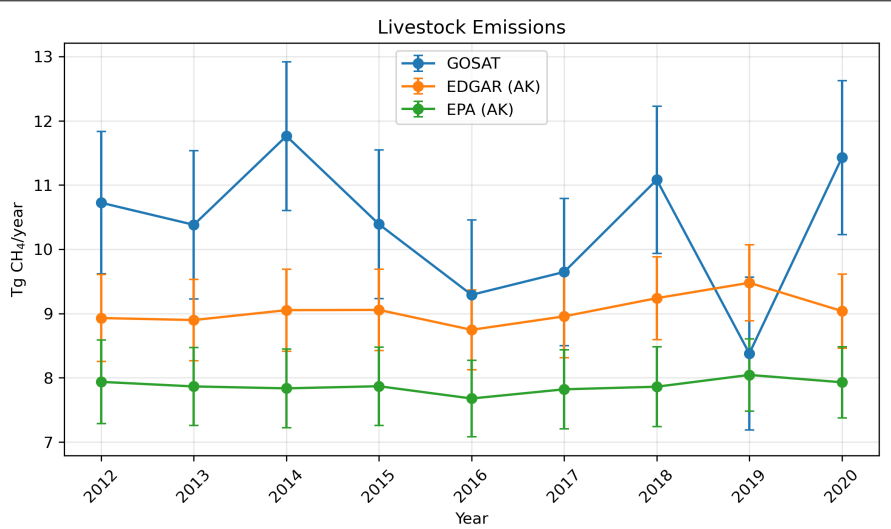


Figure 10: Integrated totals for Livestock Emissions between 2012 and 2020. The inversion operator has been applied to the inventories.

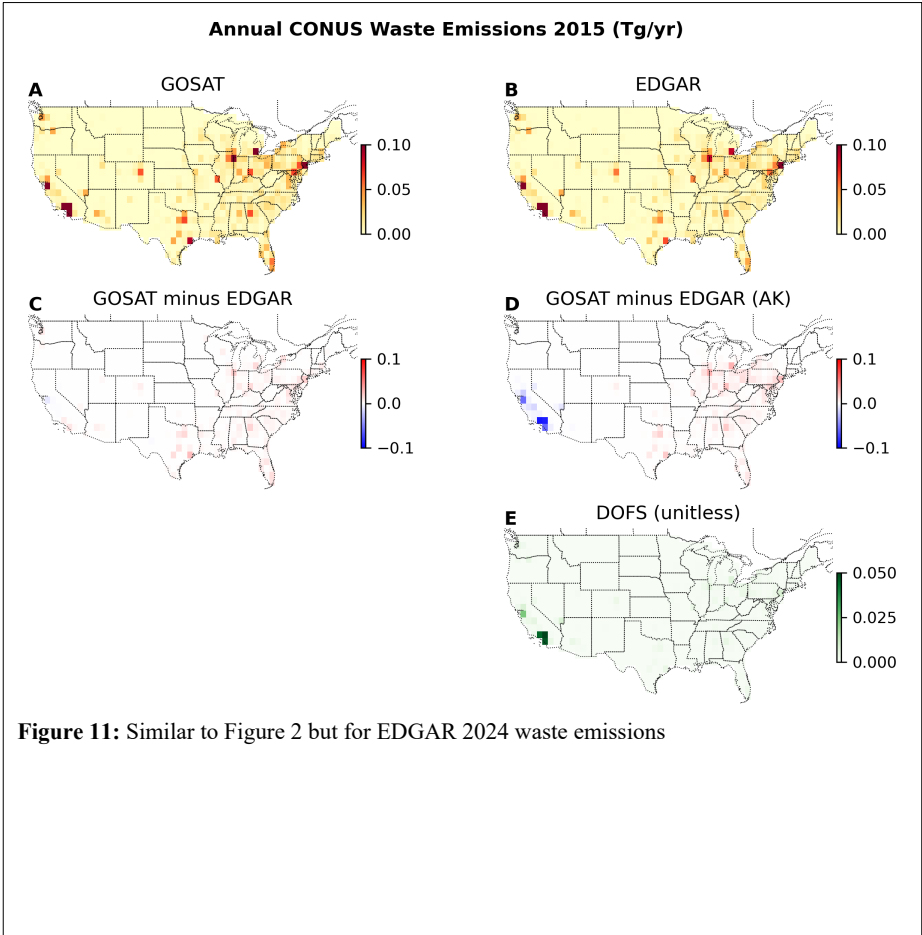
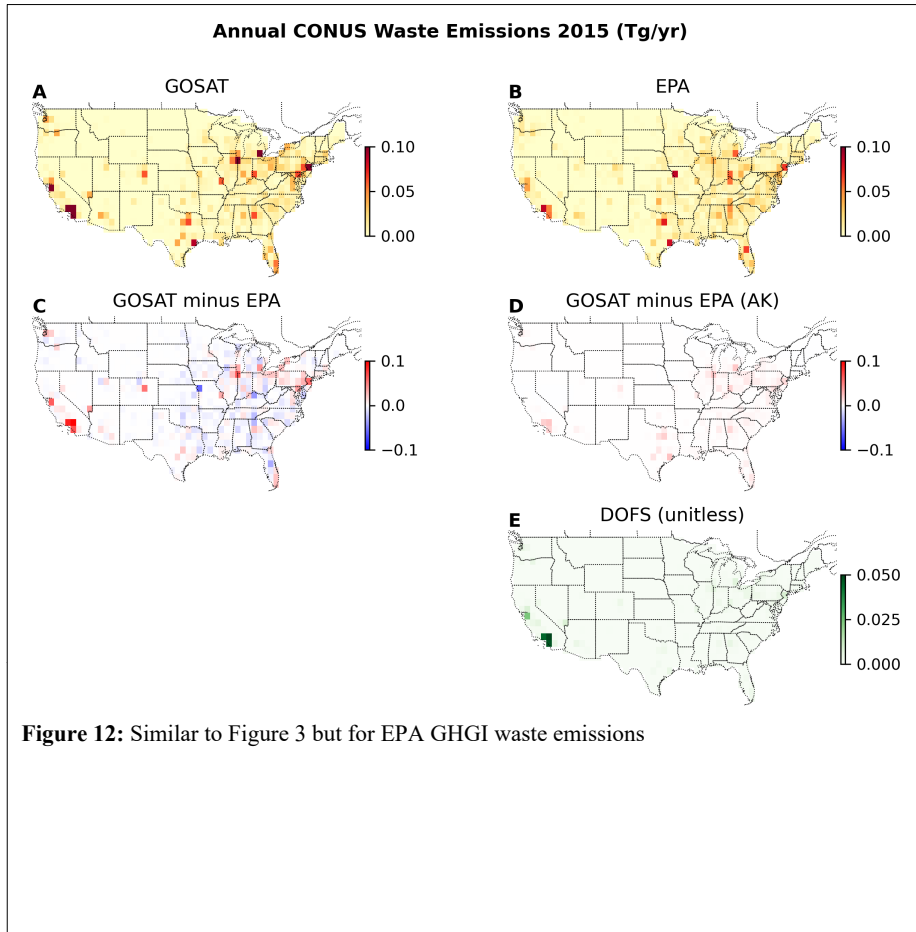


Figure 11: Similar to Figure 2 but for EDGAR 2024 waste emissions

1034
1035
1036
1037



1038
1039
1040
1041
1042
1043

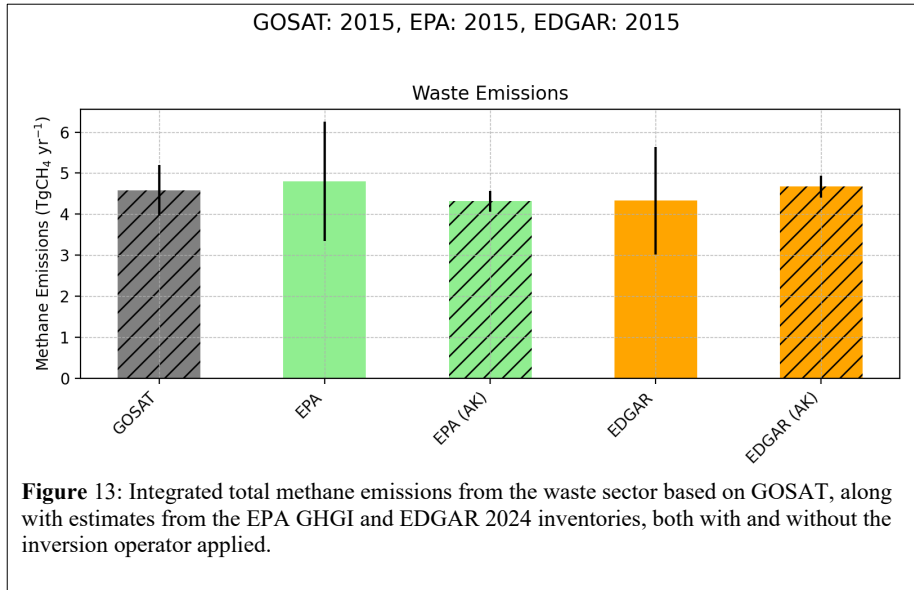
Figure 12: Similar to Figure 3 but for EPA GHGI waste emissions

1044

1045

1046

1047



1048

50

